HEAVY ION RUTHERFORD BACKSCATTERING WITH A TIME OF FLIGHT DETECTOR SYSTEM

Thesis by

Philip Charles Haubert

In Partial Fulfillment of the Requirements
for the Degree of
Doctor of Philosophy

California Institute of Technology
Pasadena, California

1990

(Submitted August 24, 1989)

Abstract

Heavy Ion Rutherford Backscattering Spectroscopy uses a beam of energetic ions to probe the composition of a surface or thin film. It has been used on a variety of systems to solve a variety of problems. In this thesis we describe a silicon surface barrier detector system and a time of flight detector system that have been built and used for several examples. These include, for example, the concentration depth profiling of thin-film high-critical-temperature superconductors and indium gallium arsenide quantum wells and superlattices. Temperature dependent electronic sputtering of VO_2 has been observed by measuring the sputtered vanadium with this technique. Software has been developed to analyze Heavy Ion RBS and ToF Heavy Ion RBS rapidly. The usefulness of the Heavy Ion RBS technique in general and of ToF Heavy Ion RBS in particular has been amply demonstrated by these examples, and the potential of the method for solving other analytical problems has been enhanced by the improvements we have made.

Contents

1 Experimental Setup **1**

1.1 Introduction 1

1.2 Heavy Ion RBS 3

1.3 Heavy Ion RBS Using ToF 4

2 Analytical Treatment **6**

2.1 TRUMP 6

2.2 ToF 11

2.3 Other Details of Heavy Ion RBS Spectral Analysis 12

3 Applications **15**

3.1 Calibration Targets 15

3.2 $In_xGa_{1-x}As$ 16

3.2.1 Multi-Layer $In_xGa_{1-x}As$ Heterojunction Quantum Well Superlattices 17

3.2.2 Thin Layer $In_xGa_{1-x}As$ Quantum Wells 18

3.3 High T_c superconductors 20

3.3.1 $Ba_2YCu_3O_{6+x}$ 20

3.3.2 $Bi_2Sr_2CaCu_2O_8$ 21

3.4 VO_2 22

3.5 Summary and Outlook 25

Chapter 1

Experimental Setup

1.1 Introduction

From noble beginnings at the origin of nuclear physics, Rutherford Backscattering Spectroscopy has evolved into a mature and versatile analytical technique. Thicknesses and concentration profiles can be measured with RBS, even crystal perfection can be probed using Channeling RBS. No particular target species is necessary; any monoatomic ion producible can be scattered. Likewise, the technique is not dependent on a particular bombarding energy, except that the energy must be low enough to be below the Coulomb barrier and the recoil energy must be high enough to be above the noise level in the detector. The technique is relatively nondestructive, with the caveat of possible sample modification.

RBS consists of the penetration of a surface by an energetic particle, the elastic recoil off a target atom heavier than the incident particle, and the subsequent exit of the particle from the target. The energy of the backscattered particle is then measured. A calculable kinematical factor (equation 2.14) allows the determination of the target species. Stopping cross sections allow determination of layer thickness. Finally an empirical scattering cross section (equation 2.13) allows the determination of a concentration profile.

Heavy Ion Rutherford Backscattering Spectroscopy refers to the use of an incident beam of particles heavier than the commonly used He. The ubiquity of the employment of that beam is due to the good energy resolution when combined with

the inexpensive and convenient solid state detectors. However, in other respects the alpha particle is inferior to its heavier cousins. The kinematic factor implies larger mass separations for heavy ions; stopping powers, which increase with Z, give better depth resolutions; the Z^2 dependence of the scattering cross section means a higher count rate for a given current close to the peak in the stopping power and the greater penetration allows thicker layers to be measured. The Z dependence on the Coulomb barrier allows the use of these higher energies. For these reasons the technique is becoming increasingly popular. [34]

One difficulty with RBS in general and Heavy Ion RBS in particular lies in the accuracy of the stopping powers used for the analysis. This uncertainty folds into the uncertainty in the target density, which is also sometimes hard to determine accurately when calculating the depth scale of a spectrum. Good current integration is necessary for the determination of absolute concentrations, although a knowledge of the target composition can often be substituted for this. Effects such as channeling and target roughness can make the interpretation of the spectrum more difficult. Finally, it usually helps if the substrate is lighter than the species of interest and, to avoid charge buildup on the target, it should be conducting.

Besides equipment expense, the major factor restraining the heavy ion technique is the poor energy resolution of heavy ions in solid state detectors. Heavy ion induced damage in the detector also results in a limited detector lifetime. A Time-of-Flight system actually gives better energy resolution with heavy ions and can last a long time with little loss of resolution.

In this work:

- Depth profiling of superlattices and quantum wells composed of $In_xGa_{1-x}As$, an important though still experimental semiconductor material, is performed with the goal of improving the fabrication process. A comparison between the old surface barrier detector instrumentation and the new TOF detector is undertaken.

- The technique is used to investigate the merits of ways to produce $Ba_2YCu_3O_{6+x}$

and $Bi_2Sr_2CaCu_2O_8$ in thin films, with the intent of finding a commercially practical method of fabrication.

- Setups for Heavy Ion RBS are described, using a surface barrier detector and a ToF detector. The ToF detector represents a major improvement in instrumentation for the technique.

- Algorithms, realized in computer code, for the rapid and accurate analysis of Heavy Ion RBS and ToF Heavy Ion RBS are presented.

- Finally, the technique is used as an analytical tool in a preliminary sputtering experiment involving the conductivity transition in VO_2.

1.2 Heavy Ion RBS

The experiments were carried out on the California Institute of Technology's 6 MV Tandem Van de Graaff Accelerator. The heavy ions used were Cl and O. The energy resolution of the sector analyzing magnet was better than 0.1%. The scattering chamber was pumped by means of a diffusion pump, and employed a liquid nitrogen cold trap to help pumping and reduce hydrocarbon buildup. A pressure of better than 1×10^{-6} Torr was maintained during the runs.

The setup is shown in figure 1. An Al enclosing can and a circular plate attached to the bottom of the target holder were used to collect secondary electrons. Enough high energy electrons are produced from the target in these experiments that biasing alone is not enough to get good current integration. A negatively biased collimator and one at ground potential are mounted upstream from a large solid angle annular surface barrier detector. Pulse pileup rejection electronics were available in the setup [31], but were needed only in the analysis of sputtering collector foils where the substrate count rates become appreciable. Current integration for this setup was typically better than ten percent. The backscatter angles into the detector ranged from 172° to 175°; the solid angle was 8.18 millisterradians.

The targets were mounted on a holder whose vertical rotation was controlled by

an external arm. The front face of the holder was recessed from the axis of rotation by an amount approximately equivalent to the thickness of a typical target. This configuration is intended to keep the scattering geometry as constant as possible as the target is tilted. This cannot prevent the near edge of the spot from moving closer to the detector as the far edge moves away. In extreme cases the beam can overlap the edge or miss the target entirely.

Tilting the target increases the path length inside the target to arrive at a given depth, effectively improving depth resolution. This technique is especially useful in analyzing thin layer samples.

Heavy ion energy measurements in surface barrier detectors are subject to pulse height defects; see [11,19,27] due to recombination and nuclear stopping. This results in a variable amount of the deposited energy not being collected, thereby worsening the energy resolution of the detector.

1.3 Heavy Ion RBS Using ToF

In this setup the beam went through the central chamber to a smaller scattering chamber, as shown in figure 2. Secondary electrons were suppressed, but not collected, with a 600 Volt bias on the target holder. As a consequence the current integration was unreliable and changed drastically with target tilt, disappearing entirely beyond an angle of 60°. The holder face was recessed as in the previous setup. The front secondary electron device, SED1, was tilted so as to not block the backscattered beam. A drift distance of 82.9 cm and a timing resolution of 200 ps was achieved. The backscatter angle was 174.7 $\pm$ .6 degrees into a solid angle of .38 $mstr$.

The secondary electron devices are shown in figure 3. The SED creates a timing pulse in this manner: an ion passing through a carbon foil creates a spray of secondary electrons [29,28,8] that are collected and amplified by a pair of microchannel plates. [35] The secondary electron yield is approximately proportional to the stopping power of the ion, so a heavy ion will produce larger and more uniform pulses (for statistical reasons) than a light ion. Only electrons produced near the exit surface

escape, thus allowing thin foils to be used without an emission penalty. Thin foils are necessary to reduce energy straggling of the backscattered ion. Angular straggling is also a factor but its deleterious effect is limited by the geometry of the devices: *i.e.*, the drift time differences of the various possible paths. A sample pulse height distribution is given in figure 4.

A $\sim$ 95% transparent grid is mounted close to the foil with a large potential difference between them, the object being uniformity of electron drift times. The two microchannel plates are biased with respect to each other and rotated into a chevron configuration, so as not to allow a straight path through both. The two plates have a dual purpose: to increase the current density in the channel of the second to the point of saturation, making the pulses more uniform; and to increase the pulse height so that the pulses could be fed directly into the constant-fraction discriminator, bypassing the pulse broadening effect of an amplifier. Unfortunately, our CFDs proved unequal to the fast rise time ($< 500ps$), so that including the timing amplifiers actually improved the timing resolution.

A conical anode behind the channel plates matched impedance with the 50Ω cable and reduced reflections. The logical outputs of the CFDs were fed into a time to amplitude converter with the signal from SED1 delayed, *i.e.* SED2 was the start. A delay box and lengths of cable allowed flight times in excess of 400 ns.

If the timing resolution is expressed as $\frac{\delta t}{t}$, where δt represents the uncertainty in the start and stop points and t is the drift time, then it is clear that the detector resolution can be improved *linearly* by simply increasing the ion drift time. The obvious ways are to lengthen the flight path, use a lower energy ion, or use a heavier ion.

Solid angle goes as reciprocal path length *squared* and economy puts a limit on channel plate size, so the count rate was quite small in our ToF detector compared to our surface barrier detector. Increasing the cross section also requires low energy heavy ions. Our rates ranged from less than 1 Hz up to about 20 Hz.

Chapter 2

Analytical Treatment

In the spectra given in the figures, smoothed values are plotted in addition to the raw data. Smoothing has several uses:

1. Extract shape information from the data.
2. No assumption about a theoretical function is needed, as opposed to functional fits.
3. More accurate determination of peak, edge, or feature height than using the raw data directly.

The following iterative procedure is used [16]:

$$y_{n+1} = y_n + (y - y_n) * r \quad , \tag{2.1}$$

where the unsmoothed data array is y and the nth smoothing is y_n. The response function, r, is convoluted with the difference of the two. An initial array, y_0, must be supplied which can range in complexity from just the zero array to a 'best' localized least squares fit.

2.1 TRUMP

A program, called TRUMP, has been developed to simulate Heavy Ion RBS spectra. In addition, it is capable of calculating stopping powers and ranges as well as single layer analysis for calculating the depth and energy corresponding to a given pulse height

channel. The simulated spectrum can be displayed vs. depth, energy, or scattering energy. A separate file contains information on target composition and structure. Isotopic and density information is optionally supplied.

Stopping cross-sections, both electronic and nuclear, are calculated using a routine given by Ziegler [39,38]. The stopping powers are calculated elementally, fitted, and then added linearly, *i.e.* Bragg's law, to arrive at a compound stopping power. The resulting coefficients are algorithmically inverted and integrated, giving the coefficients of a function of areal depth vs. energy. An areal thickness is the number of atoms per unit area.

In addition to the numeric approximations for stopping, linear additivity, and the screened Rutherford approximation to the scattering cross-section, a small beam spot and detector solid angle are assumed. Beam width, straggling, and beam attenuation with depth are not taken into consideration, but these effects could be easily added when required.

All fits are accomplished using Chebyshev coefficients. The routines come from Numerical Recipes [24], both for fitting and manipulation. Stopping powers, depth scales, and scattering energies are fitted, normally with fifty coefficients. Stopping powers are fitted once for each element and combined once for each layer type. To speed backscatter calculation, depths and energies at interfaces and previous and intermediate solutions of $f(e) = 0$ are stored. See equation 2.3 .

The height of a spectrum, aside from geometrical factors, depends on the cross-section and the areal channel width, both of which can be calculated if the scattering energy is known. The thickness is calculated from the energy loss. Thus, the calculation of backscattering basically reduces to finding a polynomial fit to the energy before scattering.

The equation of motion is:

$$a = \int_{e_1}^{e_2} \frac{da}{de}(e)\, de = \int_{e_1}^{e_2} \frac{1}{\varepsilon(e)}\, de = g(e_2) - g(e_1) \tag{2.2}$$

that is, an areal depth of a is covered in decreasing the ion's energy from e_2 to e_1, given an areal stopping cross-section of ε. The equation is solved by setting

$$f = -a + g(e_2) - g(e_1) \tag{2.3}$$

then solving for $f(e) = 0$ using a hybridized Newton-Raphson and bisection method. This function is amenable to rapid numeric solution.

In the following cases e is the energy to be obtained, e_H an energy at an interface higher than e, e_L an interfacial energy lower than e, k is the kinematic factor (as in equation 2.14), a an areal depth, a_l the areal width of layer l, γ the target tilt angle, and θ the angle between the incident beam and the detector. A sign convention is employed for these angles to separate the two distinct cases: target tilted toward the detector and target tilted away from the detector.

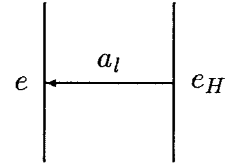

1. Energy after traversing layer:

$$\frac{a_l}{\cos\gamma} = g(e_H) - g(e) \rightarrow f(e) = a_l - g(e_H)\cos\gamma + g(e)\cos\gamma \quad . \tag{2.4}$$

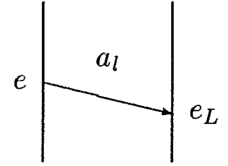

2. Energy before traverse during backscatter:

$$\frac{a_l}{\cos(\theta-\gamma)} = g(e) - g(e_L) \rightarrow \tag{2.5}$$

$$f(e) = -a_l - g(e_L)\cos(\theta-\gamma) + g(e)\cos(\theta-\gamma) \quad . \tag{2.6}$$

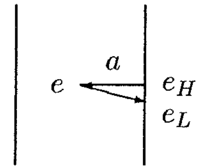

3. Energy before actual backscatter:

$$[g(e_H) - g(e)]\cos\gamma = a = \cos(\theta-\gamma)\,[g(ke) - g(e_L)] \quad ; \tag{2.7}$$

$$\rightarrow f(e) = -\cos\gamma\,[g(e_H) - g(e)] + \cos(\theta - \gamma)\,[g(ke) - g(e_L)] \quad . \tag{2.8}$$

4. Energy after traverse during backscatter:

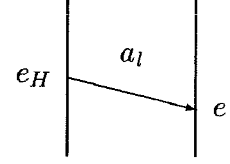

$$\frac{a_l}{\cos(\theta - \gamma)} = g(e_H) - g(e) \rightarrow \tag{2.9}$$

$$f(e) = a_l - g(e_H)\cos(\theta - \gamma) + g(e)\cos(\theta - \gamma) \quad . \tag{2.10}$$

5. Energy loss case:

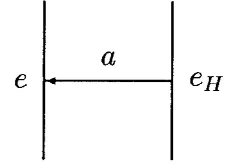

$$a = g(e_H) - g(e) \rightarrow f(e) = a - g(e_H) + g(e) \quad . \tag{2.11}$$

The simulation is mapped into a virtual multi-channel analyzer, channel vs. counts. An edge is allowed to straddle two channels or, for that matter, a layer is permitted to map entirely into a single channel. The number of counts, h, in the ith channel due to the nth element is:

$$h_{in} = f_{nl}\,Q\,\Omega\,\sigma_{zn}(s_i)\,\tau_a \tag{2.12}$$

where f is the atomic fraction, Q the fluence, Ω the detector solid angle, σ the cross-section, s the energy before scattering, τ_a the areal span of the channel in the target. The type of layer is l and the scattering ion is represented by z.

The scattering cross-section is calculated using a screened Rutherford expression:

$$\sigma_{zn}(e) = \left(\frac{ZZ_nq^2}{2e}\right)^2 \frac{\left[\sqrt{1-\frac{m_z^2}{m_n^2}\sin^2\theta}-\cos\theta\right]^2}{\sin^4\theta\sqrt{1-\frac{m_z^2}{m_n^2}\sin^2\theta}} \left[1-\frac{49}{1000}ZZ_n^{\frac{4}{3}}(1+\frac{m_Z}{m_n})\right] , \tag{2.13}$$

which is valid at energy e, high enough to penetrate the electron cloud. The angle between the incident beam and the detector is θ, q is the charge of an electron, Z and m_Z are the atomic number and mass of the ion, Z_n and m_n are the atomic number and mass of the scattering particle.

The kinematic factor, k, giving the laboratory energy after an elastic recoil, as in $e = ke_0$ is:

$$k_{zn} = \left[\frac{\sqrt{1-\frac{m_z^2}{m_n^2}\sin^2\theta}-\frac{m_z}{m_n}\cos\theta}{1+\frac{m_z}{m_n}}\right]^2 . \tag{2.14}$$

Several expressions exist for τ, the distance in a target that maps into a given channel:

$$\tau_a = \frac{s(e_{i+\frac{1}{2}})-s(e_{i-\frac{1}{2}})}{\varepsilon(s(e_i))} \tag{2.15}$$

is not well suited numerically, as it involves the small difference of two large quantities. A better expression is:

$$\tau_a = \frac{\Delta e_i \varepsilon_l^{-1}(e_i)}{\left[\frac{\cos\gamma}{\cos(\theta-\gamma)}+k_{zn}\frac{\varepsilon_l^{-1}(k_{zn}s_i)}{\varepsilon_l^{-1}(s_i)}\right]} , \tag{2.16}$$

where e_i is the exit energy and $\Delta e_i = e_{i+\frac{1}{2}} - e_{i-\frac{1}{2}}$ is the energy width of channel i, and reduces to the more familiar:

$$\tau_a = \frac{\xi}{\varepsilon(k_{zn}e_0)\sec\theta + k_{zn}\varepsilon(e_0)} , \tag{2.17}$$

where ξ is the channel energy width and e_0 the incident energy, for the case of an untilted target near the surface.

2.2 ToF

The ToF detector produces a backscattering spectrum of counts vs. time. To allow comparison with energy detectors and conventional analysis, the spectrum is converted to one of counts vs. energy. The following concerns this conversion from the time domain to the energy domain. The equation

$$t = t_0 + \tau \tag{2.18}$$

holds, where t is the observed time, t_0 is the delay, and τ is the actual time of flight. A value of $t_0 > 0$ is taken to mean that the pulses from SED2 were delayed with respect to those from SED1. In our setup $t_0 < 0$, that is, the TAC was started with events in SED2. This was done because the far lower count rate in SED2 results in less dead time in the TAC. All this means is that there are two distinct regions:

$$\begin{array}{ll} 1) & t > 0 \ \ \forall \text{ events;} \\ 2) & t < 0 \ \ \forall \text{ events (our setup).} \end{array} \tag{2.19}$$

t should not cross zero.

The basic equation of ToF is:

$$e = \frac{1}{2}mv^2 = \frac{1}{2}m\frac{d^2}{\tau^2} = \frac{md^2}{2\left(t - t_0\right)^2} = \frac{md^2}{2\left(c\frac{dt}{dc} - t_0\right)^2} \quad , \tag{2.20}$$

where e is the energy of a drifting particle, v its velocity, m its mass, d the drift distance, c the channel number, and $\frac{dt}{dc}$ the time per channel. Differentiation gives the Jacobian of the channel width transformation, and implies that the uncertainty in energy, Δe, is related to the uncertainty in time, Δt, in the following way:

$$\Delta e = -\left[\frac{md^2}{\left(c\frac{dt}{dc} - t_0\right)^3}\right]\Delta t \quad . \tag{2.21}$$

The time calibration is accomplished in one of two ways:

$$t_0 = c\frac{dt}{dc} - \sqrt{\frac{md^2}{2e}} \quad , \tag{2.22}$$

which is to say that the actual delay can be found with a knowledge of the time per channel, found by changing the delay by a known amount and noting the shift of a given peak or edge; and a point (c, e), the energy of the backscattered particles at a given peak or edge. Alternately:

$$\frac{dt}{dc} = \frac{\sqrt{\frac{md^2}{2e_2}} - \sqrt{\frac{md^2}{2e_1}}}{c_2 - c_1} \quad \text{and} \qquad t_0 = \frac{c_1\sqrt{\frac{md^2}{2e_2}} - c_2\sqrt{\frac{md^2}{2e_1}}}{c_2 - c_1} \tag{2.23}$$

are calculated by locating two peaks or edges, (c_1, e_1) and (c_2, e_2).

Values of e and t at the spectrum's endpoints, c_L and c_H, are:

$$t_L = c_L\frac{dt}{dc}, \quad e_L = \min\left(\frac{md^2}{2\left(t_L - t_0\right)^2}, \frac{md^2}{2\left(t_H - t_0\right)^2}\right) \quad \text{and} \quad t_H = c_H\frac{dt}{dc}, \quad e_H = \max\left(\frac{md^2}{2\left(t_L - t_0\right)^2}, \frac{md^2}{2\left(t_H - t_0\right)^2}\right) . \tag{2.24}$$

And the energy calibration is simply $e = a_e + b_e c$ with

$$b_e = \frac{e_H - e_L}{c_H - c_L} \quad , \quad a_e = e_H - c_H\frac{e_H - e_L}{c_H - c_L} \quad . \tag{2.25}$$

The actual conversion from time to energy domain is performed in the following way:

$$y_e = \int_{t_1}^{t_2} y_t \quad , \tag{2.26}$$

where $t_1 = t_0 + \sqrt{\frac{md^2}{2e_1}}$ and $t_2 = t_0 + \sqrt{\frac{md^2}{2e_2}}$ with (e_1, e_2) is the interval of the energy bin for a particular channel in the energy domain. y is the number of counts in a given bin of either time or energy.

2.3 Other Details of Heavy Ion RBS Spectral Analysis

First we consider the true position of an RBS feature. Consider a single layer containing an element of interest. The concentration of the element is uniform and is

present only in that layer. The finite resolution of the detector broadens the feature. At issue is the location of the edge of the layer on the spectrum. In the thin layer case the edge is at the top of a Gaussian peak, in the thick layer case the edge is halfway down the side of an error function mesa. Following [7]:

$$2h\delta = A\,\mathrm{erf}\left(\frac{\delta}{\sigma\sqrt{2}}\right) \quad , \tag{2.27}$$

which assumes a Gaussian response function in the detector, width σ; a symmetrical feature, *i.e.* no straggling, constant cross-section, and a tight geometry; and a uniform concentration profile with sharp transitions to zero at the edges. A is the area, in counts, under the feature; h the height, in counts; and δ is the number of channels from the center of the feature to the true edge.

Second, let us calculate a correction factor for the case of an annular detector in use with a tilted target. The incident path length in the target is $d \sec\gamma$ where d is the depth at which scattering takes place, measured normal to the surface, and γ is the target tilt angle. The angle between incident and scattering paths is taken to be θ and the azimuthal angle is taken to be ϕ. If the exit path length is represented by $d\Upsilon(\theta,\phi)$ it is easy to show that

$$\Upsilon(\theta,\phi) = \cos\theta\sec\gamma + \tan\theta\sec\gamma\sqrt{\sin^2\theta + \tan^2\gamma\cos^2\phi} \quad , \tag{2.28}$$

and averaging over the entire detector acceptance angle:

$$\Upsilon_{av} = \frac{1}{(\phi_2-\phi_1)}\frac{2}{(\tan^2\theta_2 - \tan^2\theta_1)}\int_{\theta_1}^{\theta_2}\int_{\phi_1}^{\phi_2}\Upsilon(\theta,\phi)\tan\theta\sec^2\theta\,d\theta\,d\phi \quad , \tag{2.29}$$

with $\Upsilon_{av} = \sec(\theta_{eff} - \gamma)$. Using

$$d = \frac{e_0 - e}{\varepsilon(e_0)\sec\gamma + \varepsilon(e_1)\sec(\theta-\gamma)} \quad , \tag{2.30}$$

with θ and d the scattering angle and path length in the case of a nonannular detector and small solid angle allows the effective scattering path length and angle to be expressed as

$$\frac{d_{eff}}{d_0} = \frac{1+\beta}{1+\beta\frac{\sec(\theta_{eff}-\gamma)}{\sec\gamma}} \quad , \tag{2.31}$$

where $\theta = 0$ gives d_0 and $\beta = \frac{\varepsilon(e_1)}{\varepsilon(e_0)}$ and the stopping powers are assumed to be constant before and after scattering.

Chapter 3

Applications

In this chapter various applications of Heavy Ion RBS are described. These include depth profiling of In for $In_xGa_{1-x}As$ superlattices and quantum wells. Results for analysis of $Ba_2YCu_3O_{6+x}$ and $Bi_2Sr_2CaCu_2O_8$ high T_c superconductors are also given. Finally there is a short description of a VO_2 sputtering experiment and the subsequent Heavy Ion RBS analysis.

3.1 Calibration Targets

A number of calibration targets were made. Most were made via evaporation by resistive heating. For example, see figure 5. Using a 16 MeV O beam, this run demonstrates the best resolution achieved with heavy ions into a surface barrier detector. The resolution of the peaks range from 31 to 50 keV, averaging 38 keV. The data suggest an energy dependence of 2–3 keV per MeV, an indication of plasma recombination. This energy resolution allowed the separation of the copper isotopes, ^{63}Cu and ^{65}Cu as well as those of silver, ^{107}Ag and ^{109}Ag. The two silver isotopes are about 100 keV apart.

A similar sample is shown as measured with the TOF system, figure 6. Using this target the energy resolution has been calculated to be $\sim$ 10 keV below 2 MeV Cl up to 42 keV for 12.7 MeV. For a 25 MeV Cl beam this puts the energy resolution of $GaAs$ at about 15 keV and of In below 25 keV. The individual contributions to the total are from timing resolution (200 picoseconds), differences in the various possible pathlengths between the two foils ($\sim 2.5mm$), and uniformity of and straggling in the

first pick-off foil ($5\mu g/cm^2$). Adding in the ordinary RBS considerations for resolution to this energy dependent ToF energy resolution makes the choice of the optimal energy and composition of the incident beam even more complicated. Accumulation times on the order of an hour were needed for these spectra, mostly due to the solid angle being only .38 $mstr$ (vs. 8 $mstr$ for the surface barrier detector setup).

A repetition of 1000 Å ($x = .1$) $In_xGa_{1-x}As$ layers over 1000 Å $GaAs$ layers on a $GaAs$ substrate was made by Molecular Beam Epitaxy at the Coordinated Science Lab at Illinois, as were all of the $In_xGa_{1-x}As$ samples. This layer thickness was chosen as a convenient, easily resolvable value. The target proved invaluable during the ToF detector testing, producing a reasonable count rate (from the $GaAs$ substrate), and allowing a monitoring of resolution and efficiency vs. energy. Such thick layers are also relatively insensitive to hydrocarbon buildup from long bombardment. The thin layer calibration target needed to be cleaned from time to time.

3.2 $\mathbf{In_xGa_{1-x}As}$

Semiconductor heterojunctions have generated a great deal of interest. [21] A particularly exciting material is $In_xGa_{1-x}As$. [2,4,10,25,20]

At the interface of two different semiconductors there is, in general, a bandgap discontinuity. If the strain induced from lattice mismatch is unrelieved by dislocations then a further bandgap change occurs. Multiple repetitions of this produce a strained layer superlattice, with bandgap tailoring possibilities and properties of a long period lattice. Also important is that the electron mobility for $In_xGa_{1-x}As$ can be nearly twice that of the already high $GaAs$. Optical waveguides, injection lasers, low-noise photodetectors and fast optical interfaces ($\sim 1GB/s$) for fiber communications, bipolar transistors ($\sim 30ps$ switching times), fast RAM ($< 1ns$ access time) based on modulation doped FETs, phototransistors, photovoltaic solar cells, and light-emitting diodes have all been constructed. With all this structural complexity, characterization is an ongoing problem.

X-ray Rocking Curve Analysis can give the strain in a superlattice, and Photo-

Reflectance measurements [18] can give the bandgaps. Neither is capable of determining directly the concentration profiles. Nuclear Resonant Reaction Analysis produces this information but a suitable reaction must be found, for example, protons onto Al in $Al_xGa_{1-x}As$. [36] Knowledge of the depth profile is important not only in determining the calibration and quality of the manufacturing process but also for the analysis of the other techniques. Heavy Ion Rutherford Backscattering is capable of producing such information.

3.2.1 Multi-Layer $In_xGa_{1-x}As$ Heterojunction Quantum Well Superlattices

These were the first samples measured. A 25 Mev Cl beam and an annular surface barrier detector were used. The resultant depth scale allowed the profiling of the entire superlattice; however, the energy resolution was not sufficient to resolve individual layers. One of these runs is shown in figure 7. This same sample was measured with the ToF detector, when it was ready. Plotted are 25 MeV Cl, figure 8, 5.5 Mev O, figure 9, and 6 MeV Cl, figure 10. A comparison of the stopping powers for the two beams is given in figure 11.

The good statistics for the low energy oxygen run suggest an attempt at further analysis. There are two competing effects here: as the projectile penetrates deeper into the target it straggles more, but its lower exit energy will result in longer drift times and thus better energy resolution. Equation 2.21 gives the dependence of energy resolution upon timing resolution. The Bohr relation for straggling is:

$$(\delta e)^2_{strag} = 4\pi z^2 q^4 NZx = \kappa^2 x \quad , \tag{3.1}$$

with δe the spread in energy after traveling a distance x, q the charge on the electron, N the atomic density, and Z and z are the atomic numbers of the ion and the target respectively.

Using a simple model of overlapping Gaussians of width δe, height H, valley height h, and separated by Δe_l, the distance between consecutive indium layers implies:

$$\delta e = \frac{\Delta e_l}{\sqrt{8 \ln \frac{2H}{h}}} \quad . \tag{3.2}$$

To find Δe_l a relation between Δe, the exit energy separation, and Δx, the interior separation which employs a mean value approximation for the stopping powers is:

$$\Delta e \simeq [k\varepsilon_{in} + \varepsilon_{out}]\Delta x \quad , \tag{3.3}$$

with k the kinematic factor, equation 2.14, and ε_{in} and ε_{out} are the stopping powers before scattering and after scattering, respectively.

This simple analysis was applied to the three runs mentioned above. A method of non-linear least squares was used to solve for δt and κ. The results are given in figure 12 and figure 13. Figure 12 gives stopping powers, exit energy separation per unit of depth, separation of adjacent layers in energy, straggling, time resolution, and reduced χ^2 of the fit. Figure 13 gives the energy resolution as calculated from equation 3.2, the value arrived at from the fit, the contribution to this resolution by the ToF detector as in equation 2.21, the contribution from straggling, and the depth resolution. The values are given for each of the layers analyzable for the three runs. The values for the timing resolutions are consistent with those from a thin layer calibration sample measured along with the superlattice. The Bohr relation gives values for straggling of 103 keV/$\sqrt{\mu m}$ for Cl and 49 keV/$\sqrt{\mu m}$ for O. These resolutions compare favorably to the numbers from the Cl run into a surface barrier detector, $\delta e \simeq 170$ keV and $\delta x \simeq 300$ Å.

3.2.2 Thin Layer $\mathrm{In_xGa_{1-x}As}$ Quantum Wells

Samples composed of a thin layer of $In_xGa_{1-x}As$ epitaxially grown on $GaAs$ were analyzed using Heavy Ion RBS. An equal number were analyzed that had had a 300Å $GaAs$ layer grown on top of the $In_xGa_{1-x}As$. The layer thicknesses were 100, 200, and 300 Å, the In concentrations were $x = .1, .15,$ and $.2$. Together with the buried and unburied cases this gives eighteen samples.

The Si surface barrier detector setup was first used. The beam was chosen to be 25 MeV ^{35}Cl. The total dose was 2.5×10^{13} ions in a spot about $\sim 1mm$ by $1mm$.

The beam current ranged from $\sim$ 10–50 nanoamperes. The pressure during the run was better than 1×10^{-6} Torr.

Accidental channeling proved to be a problem, decreasing the backscattered yield by $\sim$ 40%. An angular channeling scan is given in figure 14. *GaAs* has planar channels in the x and the y directions. To reduce the channeling the targets were mounted rotated 9° in the $x - y$ plane and tilted with the target holder arm during the actual run. Two runs were done for each sample: one at 6° tilt and one at 78.5° tilt.

The positions of the edges were found using equation 2.27. Results are given in figure 15. Applying the annular detector correction from page 13 with γ =–78.5° and $\beta \simeq$ .63 gives $\theta_{eff} = 3.06°$ and $\frac{d_{eff}}{d_0} = .878$, *i.e.*, the results as calculated should overestimate, due to target tilt with an annular detector, the actual thicknesses by at most 14%.

The results from backscattering with the same beam using the ToF system are given in figure 16. An example of each is shown in figure 17. The superior statistics of the surface barrier detector cannot compete with the far better depth and energy resolution of the ToF detector. The poor statistics limit the ability to do concentration profiling; the excellent depth resolution (~10 Å) is only fully realizable at a point where the concentration goes from zero to some finite value.

Layer thicknesses, however, can be accurately determined. During the analysis varying the tilt angle demonstrated that some light material was present on the surface. The analysis represents this layer as hydrocarbons. A thin layer calibration standard (YACS) gave the time calibration for each day. At the left of each spectrum are the As and Ga edges, the height of which give the total particles incident (because accurate current integration is not yet possible with this setup) and the position of which give the carbon buildup. To the right on the spectrum is the In feature. The depth scale is for ^{115}In, with zero being the surface of the target. Unlike the surface barrier detector measurements, the spectra are easy enough to interpret visually.

With a thin layer of *GaAs* on top of a lighter substrate, an accurate ratio of Ga to As may be determined. Such an example is shown in figure 18. The two isotopes

of Ga result in two peaks; the width and step structure of the Pd feature is due to its isotopes. Note the diffusion of the Ga and As into the Pd layer. This layer is intended to form a contact with the *GaAs* layer. The Ga has diffused somewhat more readily than the As.

3.3 High T_c superconductors

These samples were made by the Jet Propulsion Laboratory and Rockwell International Science Center. The Heavy Ion RBS setup with an annular surface barrier detector was used for these measurements. The vacuum was maintained at better than 1×10^{-6} Torr. The densities were roughly calculated from a linear sum of the component oxides as in

$$\rho = \frac{N}{F} \sum f_i n_i \frac{g_i}{A_i} \quad , \tag{3.4}$$

where ρ is the compound's atomic density, atoms$/cm^3$, the sum is over all components, g is in g/cm^3, A is the molecular mass, $g/$mole, n is atoms/molecule, N is Avagodro's number, and $F = \sum f_i$. Later values were arrived at from x-ray crystallographic data, using a $\theta/2\theta$ diffractometer.

These samples represent attempts to figure out ways to make thin film superconductors of better crystalline quality, for instance by reducing the required annealing temperature. The heavy ion mixing observed could allow the construction of integrated circuits with superconducting connections.

3.3.1 $Ba_2YCu_3O_{6+x}$

The first sample was an unannealed structure consisting of 27 layers of the components of the superconductor; nine repetitions of $Y/BaF_2/Cu$. The beam used was 25 Mev Cl, the substrate was Si. During the analysis, the Ba peaks broadened. The sample was moved to a new spot and as short a run as was practical was performed, a dose of 1.5×10^{12} incident ions, as shown in figure 19. The dose was increased and again the smearing of features was observed, attributable to ion beam mixing. [12] The final run, given in figure 20, was started at a total dose of 2.7×10^{13} ions and ended at a

total dose of 4.95×10^{13} ions. In both cases the area of beam spot was on the order of $1mm^2$.

The next pair of $Ba_2YCu_3O_{6+x}$ samples were intended to be half a micron thick. Analysis with a 16 MeV oxygen beam indicated that they were at least twice that thick, however. The results are shown in figure 21. The overall normalization of the second is noticeably worse than the first. This discrepancy could be due to an error in the current integration or the contamination of the sample by some lighter material.

The final $Ba_2YCu_3O_{6+x}$ sample was good quality, judging from visual and SEM inspection. The transition temperature was fairly broad at about 70° K; the critical current density was relatively high. During deposition a beam of O was held on the sample to increase the O content in the final superconductor. The substrate was held at an elevated temperature during deposition so that a lower annealing temperature could be used. A Heavy Ion RBS spectrum is shown in figure 22, taken with a 16 MeV oxygen beam. The value of x in the formula $Ba_2YCu_3O_{6+x}$ was taken to be 0.5. A small amount ($\sim$ .05%) of contamination by a heavy element (either Ta or W) was observed. Also present was a similar amount of light element contamination.

3.3.2 $\mathbf{Bi_2Sr_2CaCu_2O_8}$

These two samples were sputter deposited with an Ar beam of keV energy using knowledge of the different sputtering yields. The sputtering chamber was Cu lined to reduce contamination from stray sputtered material. An ambient pressure of 4×10^{-4} Torr of O_2 was maintained during deposition. The transition temperature was only 55–60° K. The analysis was conducted with 16 MeV oxygen. Figures 23 and 24 plot the results of these measurements. The transition temperature indicates that the structure present is $Bi_2Sr_2CaCu_2O_8$. SEM studies [17] suggest single phase and show the presence of Ca_2CuO_3 chunks of $\sim .5\mu m$ on the surface. In this material, Ca is capable of replacing Sr in the lattice — this process is assumed in the analysis in addition to the presence of the Ca_2CuO_3 chunks. Taking these assumptions concerning composition into account leaves a significant amount of excess Cu. The oversized tails in the Cu features indicate the possibility of diffusion into the sub-

strate. It was then discovered that makers of this material routinely overdeposit Cu during the sputter deposition. The size of the Cu atom is comparable to the lattice spacing in the MgO substrate and smaller than the other elements comprising the superconductor, suggesting its diffusivity to be significant as well as greater than the other elements. It would be possible to test this hypothesis of diffusion by changing the annealing temperature or the annealing time.

3.4 VO_2

If a material is subjected to ion bombardment, atoms are observed to leave the surface. This process is known as sputtering. Energy transfer is necessary to produce sputtering and consequently it may be categorized in a similar manner as the stopping cross section: nuclear and electronic. Nuclear scattering allows momentum to be transferred directly; electron scattering produces the excitation of electrons, which is an intermediary to the atomic ejection. The premise of energetic electron scattering allows the construction of a simple model. The scattered electrons leave behind a positively charged region along the ion path. Adding the further requirement of a certain energy density beyond which sputtering is constant, then Maxwell's equations give a sputtering yield, Y, of

$$Y = \frac{P_0 \lambda^2}{16\pi\sigma u_0} \tag{3.5}$$

with λ representing the line charge deposited along the track, u_0 the threshold energy density for sputtering, σ the conductivity, and P_0 the probability of sputtering per area per time. Electronic sputtering should vary inversely with the conductivity.

VO_2 has a conductivity that varies with temperature, as shown in figure 25. The transition is comfortably above room temperature but low enough to be easily obtainable. The preceeding suggests that if electronic processes are enhanced over nuclear ones then the same material can exhibit widely differing sputtering yields at different temperatures. An experiment was conducted to investigate this contention.

The apparatus used is described in [31]. A foil is mounted in front of the target to collect the sputtered particles. A cylindrical holder positions this foil to allow a

number of runs. Holes in the foil allow the passage of the beam. Thus the data from this experiment is in the form of a small amount of material deposited in bands on the foil. Each band gives the differential yield in the horizontal plane at angles ranging from $\sim 12°$ to $90°$ on either side of a hole. To convert this data to a more easily understood form the material on the foil must be measured. Heavy Ion RBS is a good technique for doing this.

The VO_2 sample was a 1600 Å layer grown on a sapphire substrate. It was mounted in the chamber and evacuated. To eliminate contamination from pump oils, a sorption pump was used to rough the chamber and an ion pump thereafter. The chamber was not baked, because of concerns over the VO_2 reacting with residual contaminants. Before runtime the pressure was better than 5×10^{-9} Torr, increasing with bombardment and heating into the low 10^{-8} Torr range. A heater was clamped to the target block and external leads were available for measuring resistance *in situ*.

A 25 MeV Cl beam was chosen to maximize the energy loss and consequently the sputtering yield. The nuclear component of the stopping cross section is about a quarter of a percent of the electronic at this energy. A run at room temperature (insulating phase) was made and then the temperature was raised to 75° C and a similar run was made at the same spot. Keeping the temperature elevated, the sample was moved to a new spot and a high and then a low temperature run were made. Finally, this same spot was irradiated with 10 keV Ar beam, which is near the maximum of yield for nuclear sputtering.

The foils were analyzed using the Heavy Ion RBS setup of figure 1 except that the foil was mounted on a cylinder that fit inside the can, bringing the solid angle up to 50 millisterradians. A 16 MeV beam of O was used to separate the V peak from the scattering from the Al substrate. Foils with very low impurity levels are required for this experiment. No drop in the count rate with time was seen, which would have indicated resputtering of the V from the foil. Unit sticking probability is assumed for this analysis, a low coefficient — as for example with silver [33] — makes the angular results inconclusive. The pulse pileup rejection and dead time analysis parts of the setup were used.

Results of the analysis are shown in figure 26. An angular scan was performed for runs 1 and 3, the results are given in figure 27 and plotted in figure 28. The sputtering yield between the cold and hot cases differs by an order of magnitude. A temperature dependence was seen.

The measured resistance across the sample indicates which state that it is in, but the contacts were not reliable enough for absolute numbers. The day before the runs the resistance for the cold and hot cases was 120,000 and 10,000 Ohms, respectively. On the day of the runs these values were 160,000 and 3500 Ohms. After the bombardments, the values were 120,000 and 2500 Ohms. A flaw in the temperature regulation system caused the temperature during the second run to rise to 128° C; fortunately the sample can withstand 200 or 300° C. Measurements of the conductivity during and after the runs showed the bulk to be undamaged but the spots to be poorer conductors. Consequently runs 2 and 4, performed on an already damaged spot, are difficult to interpret.

The yield for run # 1 is greater than for run # 3; likewise the yield for run #2 is greater than for run # 4. This suggests that damage in the insulating phase makes the conducting phase more insulating and that damage in the conducting phase makes the insulating phase more conducting. A series of resistance vs. damage measurements has been done, which confirms these hypotheses up to about $10^{14}\frac{atoms}{cm^2}$.

Because the layers on the foil are so thin (much less than a monolayer) the data analysis is simple. The differential yield is

$$\frac{\partial Y}{\partial \Omega} = \frac{r^2}{N_0 Q \Omega \sigma} S \quad , \tag{3.6}$$

with $\frac{\partial Y}{\partial \Omega}$ being the (angular dependent) average number of particles sputtered into a unit solid angle for each incident ion. N_0 is the total number of incident ions in the sputtering experiment, Q the total ions in the Heavy Ion RBS analysis, r the distance from the target to the collector foil in the sputtering experiment, Ω the solid angle in the analysis, σ the scattering cross section in the analysis, and finally S is the counts in the (Vanadium) peak in the analysis.

It seems clear that the expected dependence of the electronic sputtering yield on conductivity has been confirmed; however, the interpretation of the angular distribution observed is complicated by the crystalline nature of the VO_2 (channeling of the sputtered atoms) and possibly by redistribution due to a non-negligible possibility of vanadium atoms not sticking to the collectors on the first impact.

3.5 Summary and Outlook

Rutherford Backscattering Spectroscopy is a well known and widely used technique in surface analysis. The advantages of using heavy ions have been amply demonstrated: larger mass separation; better depth resolution; and higher count rate. The disadvantage of poor detector resolution has been overcome with the ToF detector. The detector system has been built and tested; its superiority over surface barrier detectors for heavy ion detection has been shown.

Thin film high T_c superconductors and $In_xGa_{1-x}As$ structures have been depth profiled with the goal of improving the fabrication of the materials to move toward eventual commercialization.

Software has been developed to aid in the data analysis of Heavy Ion RBS and ToF Heavy Ion RBS, with the goals of speed, accuracy, and convenience.

The large scattering cross sections, allowing small amounts or impurities to be detected, makes the technique suitable for the analysis of sputtering experiments. A material, VO_2, with conductivity-dependent sputtering behavior has been presented as an example of another way that this analytical technique can be exploited. The VO_2 system is undergoing further investigation.

A great number of surface analysis techniques now exist, each with their own strengths. Applying a smorgasbord of techniques gives a detailed picture of the structure and material properties of a sample. Heavy Ion RBS is a general technique that provides information that many others cannot. The equipment and personnel now exist to attack a wide variety of surface analysis problems. The future of the technique appears very bright.

Bibliography

[1] G. Beck. Photodiode and holder with 60 psec response time. *Rev. Sci. Instrum.*, 47(7):849–853, July 1976.

[2] Pallab K. Bhattacharya, Utpal Das, F. Y. Juang, Yasunobu Nashimoto, and Sunanda Dhar. Material properties and optical guiding in *InGaAs-GaAs* strained layer superlattices — a brief review. *Solid-State Electronics*, 29(2):261–267, 1986.

[3] J. David Bowman and R. H. Heffner. A novel zero time detector for heavy ion spectroscopy. *Nuclear Instruments and Methods*, 148:503–509, 1978.

[4] Kevin Brennan. Theroetical study of multiquantum well avalanche photodiodes made from the *GaInAs/AlInAs* material system. *IEEE Transactions on Electron Devices*, ED-33(10):1502–1510, October 1986.

[5] A. Chevarier and N. Chevarier. Time of flight spectrometry in heavy ion backscattering analysis. *Nuclear Instruments and Methods*, 218:1–5, 1983.

[6] A. Chevarier, N. Chevarier, and S. Chiodelli. A high resolution spectrometer used in MeV heavy ion backscattering analysis. *Nuclear Instruments and Methods*, 189:525–531, 1981.

[7] Wei-Kan Chu, James W. Mayer, and Marc-A. Nicolet. *Backscattering Spectrometry.* Academic Press, Inc., 1978.

[8] H. G. Cleric, H. J. Gehrhardt, L. Richter, and K. H. Schmidt. Heavy-ion induced secondary electron emission — a possible method for Z-identification. *Nuclear Instruments and Methods*, 113:325–331, 1973.

[9] Lawrence R. Doolittle. Algorithms for the rapid simulation of Rutherford backscattering spectra. *Nuclear Instruments and Methods*, B9:334–351, 1985.

[10] Mark D. Feuer, Tao-Yuan Chang, and Stephen C. Shunk. *InGaAs/InAlAs* heterostructure diodes for application to high-speed semiconductor-gated FETs. *IEEE Transactions on Electron Devices*, ED-33(11):1640–1643, November 1986.

[11] E. C. Finch and A. L. Rodgers. Measurements of the pulse height defect and its mass dependence for heavy-ion silicon detectors. *Nuclear Instruments and Methods*, 113:29–40, 1973.

[12] M. Foote, B. Hunt, R. Livi, P. Haubert, M. Döbeli, T. A. Tombrello, R. M. Housley, and D. L. Goodstein. Evolution of layered high temperature superconducting oxide precursor films under high energy heavy ion bombardment. In *Proc. of Scanning 89/EM West*, Long Beach CA, April 1989. in press.

[13] J. Girard and M. Bolore. Heavy ion timing with channel-plates. *Nuclear Instruments and Methods*, 140:279–282, 1977.

[14] G. Gloeckler and K. C. Hsieh. Time-of-flight technique for particle identification at energies from 2-400 keV/nucleon. *Nuclear Instruments and Methods*, 165:537–544, 1979.

[15] G. Gloeckler, F. M. Ipavich, W. Studemann, et al. The charge-energy-mass spectrometer for 0.3-300 keV/e ions on the AMPTE CCE. *IEEE Transactions on Geoscience and Remote Sensing*, GE-23(3):234–240, May 1985.

[16] Howard C. Hayden. Data smoothing routine. *Computers in Physics*, 74–75, Nov/Dec 1987.

[17] R. M. Housley, P. Korbin, A. Harker, P. Haubert, M. Döbeli, R. Livi, D. L. Goodstein, and T. A. Tombrello. Scanning electron microscope and Heavy Ion RBS characterization of thin $Bi - Sr - Ca - Cu - O$ films. In *Proc. of Scanning 89/EM West*, Long Beach CA, April 1989. in press.

[18] G. Ji, U. K. Reddy, D. Huang, T. S. Henderson, and H. Morkoç. Transmission and photoreflectance spectra in highly strained *InGaAs-GaAs* multiple quantum wells. *Superlattices and Microstructures*, 3(5):539–545, 1987.

[19] S. B. Kaufman, E. P. Steinberg, B. D. Wilkins, J. Unik, and A. J. Gorski. A calibration procedure for the response of silicon surface-barrier detectors to heavy ions. *Nuclear Instruments and Methods*, 115:47–55, 1974.

[20] Andrew A. Ketterson, William T. Masselink, Jon S. Gedymin, John Klem, Chin-Kun Peng, William F. Kopp, Hadis Morkoç, and K. R. Gleason. Characterization of *InGaAs/AlGaAs* pseudomorphic modulation-doped field-effect transistors. *IEEE Transactions on Electron Devices*, ED-33(5):564–571, May 1986.

[21] A. G. Milnes. Semiconductor heterojunction topics: introduction and overview. *Solid-State Electronics*, 29(2):99–121, 1986.

[22] E. Möbius, G. Gloeckler, D. Hovestadt, et al. The time-of-flight spectrometer SULEICA for ions of the energy range 5-270 keV/charge on AMPTE IRM. *IEEE Transactions on Geoscience and Remote Sensing*, GE-23(3):274–279, May 1985.

[23] Andrus Niler. *Stopping power effects on Rutherford backscattering analysis in thick targets.* Technical Report BRL–MR–3615, U.S. Army Ballistic Research Laboratory, July 1987.

[24] William H. Press, Brian P. Flannery, Saul A. Teukolsky, and William T. Vetterling. *Numerical Recipes.* Cambridge University Press, 1986.

[25] Mulpuri V. Rao, Pallab K. Bhattacharya, and Chung-Yih Chen. Low-noise $In_{0.53}Ga_{0.47}As : Fe$ photoconductive detectors for optical communication. *IEEE Transactions on Electron Devices*, ED-33(1):67–71, January 1986.

[26] Ivan K. Schuller and J. D. Jorgensen. Structure of high T_c oxide superconductors. *MRS Bulletin*, XIV(1):27–30, January 1989.

[27] W. Seibt, K. E. Sundström, and P. A. Tove. Charge collection in silicon detectors for strongly ionizing particles. *Nuclear Instruments and Methods*, 113:317–324, 1973.

[28] C. R. Shi, H. S. Toh, D. Lo, R. P. Livi, M. H. Mendenhall, D. Z. Zhang, and T. A. Tombrello. Secondary electron emission from the entrance and exit surfaces of thin carbon foils under fast bombardment. *Nuclear Instruments and Methods*, B9:263–269, 1985.

[29] E. J. Sternglass. Theory of secondary electron emission by high-speed ions. *The Physical Review*, 108(1):1–12, October 1957.

[30] T. A. Tombrello. Track damage and erosion of insulators by ion-induced electronic processes. *Nuclear Instruments and Methods in Physics Research*, B2:555–563, 1984.

[31] Duncan L. Weathers. *Sputtering by Multiply-Charged Ions, and Preferential Sputtering of Isotopic Mixtures.* PhD thesis, California Institute of Technology, 1989.

[32] A. Weber and H. Mommsen. Background in Rutherford backscattering spectra: a simple formula. *Nuclear Instruments and Methods*, 204:559–563, 1983.

[33] Martha Riherd Weller, Kevin M. Hubbard, Robert A. Weller, Duncan L. Weathers, and T. A. Tombrello. Sticking probabilities for sputtered Ag and Au atoms incident on oxidized aluminum surfaces. *Nuclear Instruments and Methods in Physics Research*, B42:19–28, 1989.

[34] Martha Riherd Weller, Marcus H. Mendenhall, Philip C. Haubert, Max Döbeli, and T. A. Tombrello. Heavy Ion Rutherford Backscattering. In *Proc. of High Energy and Heavy Ion Beams in Material Analysis*, Albuquerque NM, June 1989. in press.

[35] Joseph Ladislas Wiza. Microchannel plate detectors. *Nuclear Instruments and Methods*, 162:587–601, 1979.

[36] F. Xiong, T. A. Tombrello, H. Z. Chen, H. Morkoç, and A. Yariv. Direct determination of Al content in molecular-beam epitaxially grown $Al_xGa_{1-x}As$ $(0 \leq x \leq 1)$ by nuclear resonant reaction analysis and x-ray rocking curve techniques. *J. Vac. Sci. Technol.*, B 6(2):758–762, 1988.

[37] A. M. Zebelman, W. G. Meyer, K. Halbach, A. M. Poskanzer, R. G. Sextro, G. Gabor, and D. A. Landis. A time-zero detector utilizing isochronous transport of secondary electrons. *Nuclear Instruments and Methods*, 141:439–447, 1977.

[38] J. F. Ziegler. *Handbook of Stopping Cross-Sections for Energetic Ions in All Elements.* Pergamon Press, New York, 1980.

[39] J. F. Ziegler, J. P. Biersack, and U. Littmark. *The Stoppings and Range of Ions in Solids.* Pergamon Press, New York, 1985.

List of Figures

1. Experimental setup for Heavy Ion RBS. The downstream collimator is slightly larger than the upstream and is biased to suppress the secondary electrons from it. An enclosing can is biased to suppress secondary electron emission from the target and collects those electrons not suppressed. Pulses are fed into the circuit at the preamp and counted on the multichannel analyzer to get the percentage dead time. The MCA is gated with an inspector in order to eliminate pulse pileup. The angle and vertical position of the target are adjustable with an external arm.

2. Experimental setup for ToF, approximately 20% full size. The beam is run through a confining tube to reduce the noise in the SEDs. The pulses from SED1 are fed through a length of cable to allow the time-to-amplitude convertor to be started with SED2. The alignment of the SEDs and the beam tube was done with a laser. Even a slight misalignment drastically reduces detector efficiency.

3. Secondary Electron Devices, SED1 and SED2. The drawings are at 90% full size except for the exaggerated widths in the microchannel plate sandwich. The foil in SED1 is slanted and a slot is cut through the assembly to allow clearance for the backscattered beam. From left to right: secondary electron emission foil, acceleration grid, electron flight path, brass contact plate, first microchannel plate, an insulating separator with evaporated contacts, second microchannel plate with its channels slanting in the opposite direction, another contacting plate, conical anode, and SMA panel mount. Springs on the clamping bolts allow fine control over the contacting force on the plates.

4. A typical spectrum of pulses out of a secondary electron device. The pulses are from the rear device for 25 MeV Cl backscattering off gold. The separation of the

signal peak from the noise allows high counting efficiency with few background counts.

5. [abc] A spectrum of a thin layer calibration sample, made with an annular silicon surface barrier detector, showing the resolution of Cu and Ag isotopes. The beam was 16 Mev ^{16}O. The sample, YACS, has from top down: Bi(2.3Å), Pr(3.3Å), Ag(3.3Å), Y(4.6Å), Cu(7.2Å), Mn(14Å) evaporated onto an Al substrate.

6. [ab] A spectrum of the YACS calibration sample, made with the ToF detector. The isotopes, each representing a separation of two mass units, are well resolved. The beam was 25 Mev ^{35}Cl, the target a twin to the one in figure 5.

7. [ab] Multilayer Heterojunction using a surface barrier detector. The beam was 25 MeV ^{35}Cl. The target is 10 repetitions of $In_{.18}Ga_{.82}As$ (80Å) over GaAs (200Å) with a substrate of Si doped GaAs. The ideal spectrum is plotted with the data. The ten In layers are at the right, well separated from the Ga and As edges at the left. None of these layers are actually resolved, nor are the two Ga isotopes.

8. [ab] Multilayer Heterojunction using ToF, 25 MeV Cl. The sample and the beam are the same as in figure 7. Both the superior resolution and the lower count rate of the ToF system are clearly visible.

9. [ab] Multilayer Heterojunction using ToF, 5.5 MeV O. The sample of figure 7 as analyzed with a low energy beam of O. This energy gives a drift velocity through the detector close to that of 25 MeV Cl. The Tandem Accelerator can produce a more intense beam of O than Cl and the cross section increases with decreasing energy so the statistics are better than in figure 8. However; the In layers are not well separated from the Ga and As edges, due to the combination of beam energy, kinematical factors, and energy losses in the material. Notice how straggling increases with layer depth.

10. Multilayer Heterojunction using ToF, 6 MeV Cl. The sample of figure 7 as it appears with a low energy Cl beam. Straggling has spoiled the resolution of the deeper layers, even though the low velocity gives a good resolution of drift time. Detector efficiency is starting to drop at the region of the As edge.

11. Stopping powers of Cl and O in $GaAs$. The higher stopping power of Cl over O gives a better inherent depth resolution, but a relatively high energy must be used to get near the maximum of the curve. The nuclear component of the stopping cross section at these energies is essentially negligible.

12. Results of analysis of Multilayer Heterojunction, as described in the text, for the three cases as shown in figures 8, 9, and 10. The first four columns are stopping powers before and after scattering, at the surface and at depth. The column labeled $\frac{\Delta e}{\Delta x}$ gives the energy separation as seen in the detector per Å of target depth. Δe_l is the energy separation of the layers. κ is the fitted value of the straggling parameter, δt that of the time resolution, and χ_r^2 gives an indication of the goodness of fit.

13. Results of analysis of Multilayer Heterojunction, giving resolutions by layer. For each analyzable layer the total energy resolution is given. $\frac{de}{dt}$ is the timing resolution contribution to the energy resolution; $\kappa\sqrt{x}$ is the contribution from straggling. δx is the depth resolution.

14. Channeling scan of 25 MeV Cl onto high quality $GaAs$, using the surface barrier detector. The surface of the sample is a buried, epitaxially grown, layer of $In_xGa_{1-x}As$. Plotted are backscattered counts in a given region for a constant number of incident ions vs. the incident angle of the beam. The solid line is from the arsenic edge; the dashed line from the indium feature. The counts for the In peak have been multiplied by 10.

15. Results of the $In_xGa_{1-x}As$ quantum well analysis with a surface barrier detector. The samples were epitaxial $In_xGa_{1-x}As$ on $GaAs$ with an optional layer of $GaAs$ above. *fab* is the intended (fabricated) value, *exp* the experimental one.

x is the thickness of the $In_xGa_{1-x}As$ layer, d the depth of the layer beneath the surface, $2f$ is the same as x in the formula $In_xGa_{1-x}As$, and a is the total amount of In.

16. Results of the $In_xGa_{1-x}As$ quantum well analysis using the ToF detector. The same information as in figure 15 is tabulated except that C is the calculated thickness of hydrocarbon buildup on the surface.

17. [ab] Two spectra for the same quantum well sample, the first using a surface barrier detector, the second using ToF. The sample was 3901, nominally a 200Å layer of $In_{.15}Ga_{.85}As$. The beam in both cases was 25 Mev Cl. In the first, the In peak has been multiplied by 10 and shifted 290 channels toward the As edge. The target tilt angles were 78.5° and 72.5° respectively.

18. [ab] Thin layer of $GaAs$ buried under a layer of Pd. A 25 MeV Cl beam was used with the ToF system. Some Ga and As has diffused into the Pd. Ga and Pd isotopes are resolved. The theoretical spectrum shows a 480Å layer of $GaAs$ underneath a 260Å layer of Pd with 15% of diffused $GaAs$.

19. Unannealed $Ba_2YCu_3O_{6+x}$, deposited in layers, prior to ion beam mixing and analysis with the surface barrier detector and 25 MeV Cl ions. The sample, produced by electron beam deposition, is 9 repetitions of Y(200Å) / BaF_2(750Å) / Cu(220Å) on a Si substrate. The dose was $Q = 1.5 \times 10^{12}$ ions. Mixing and analysis were proceeding simultaneously.

20. Unannealed $Ba_2YCu_3O_{6+x}$, deposited in layers, after ion beam mixing. Layers are no longer visible. Previous to this run the total dose was $Q = 2.7 \times 10^{13}$ ions. The run itself dumped 2.25×10^{13} ions into the sample, in a beam spot $\sim 1mm^2$.

21. [ab] Thick layer $Ba_2YCu_3O_{6+x}$ samples analyzed with a 16 MeV beam of oxygen and the surface barrier detector. The substrates are MgO. The layer thicknesses are 11,000Å and 12,000Å respectively.

22. [ab] $Ba_2YCu_3O_{6+x}$, sample #111488A, produced by Ar beam sputtering and an O beam on target with the substrate held at 600°C. The annealing was for 11 hours at 450°C. A 16 MeV beam of O was used with the surface barrier detector because of the good resolution of that beam with that detector. The layer is 1760Å of $Ba_{2.07}Y_{.949}Cu_3O_{6.5}$. The substrate is MgO. An .05% impurity of either tantalum or tungsten is visible to the right of barium feature, apparently inadvertently deposited during deposition.

23. [ab] Annealed $Bi_2Sr_2CaCu_2O_8$, sputter deposited, sample #030788A. A 16 MeV beam of O was used with the surface barrier detector. The sample is a 1400Å layer of $Bi_2Sr_{1.78}Ca_{1.22}Cu_2O_8$ on MgO. Included in the analysis was 2.6% of Ca_2CuO_3 chunks observed on the surface. The diffusion of the Cu into the substrate is modeled as a 700Å 3.5% layer.

24. [ab] Annealed $Bi_2Sr_2CaCu_2O_8$, sputter deposited, sample #031088A. A 16 MeV beam of O was used with the surface barrier detector. The sample is a 900Å layer of $Bi_2Sr_{1.68}Ca_{1.32}Cu_2O_8$ on MgO. Included in the analysis was 2% of Ca_2CuO_3 chunks observed on the surface. The diffusion of the Cu into the substrate is modeled as a 600Å 3.5% layer.

25. A plot of the resistivity of VO_2 vs. temperature.

26. Results of the VO_2 sputtering experiment. N_0 is the number of incident Cl ions, $N(\theta)$ is amount of V on the collector foil, and Y is the estimated total yield. 15° and 25° refer to locations on the collector foil corresponding to those ejection angles from the sample.

27. Angular dependence of differential yield for the cold and hot runs done on virgin surfaces. $\frac{\partial Y}{\partial \Omega}$ is the number of sputtered particles per unit solid angle per incident ion. 'V' is from the counts in the Vanadium peak, 'Ni' is something about eight mass units heavier, 'W' is likewise something in that neighborhood of mass.

28. [ab] Plots of differential yield vs. angle. The dashed lines represent vanadium sputtering, the dotted lines the yield of something slightly heavier, and the solid lines are the total of the two. The solid lines at the bottom of the plots represent the presence of a small amount of material with a mass near tungsten. The plots are from the data in figure 27, the cold and hot runs respectively.

Figure 1

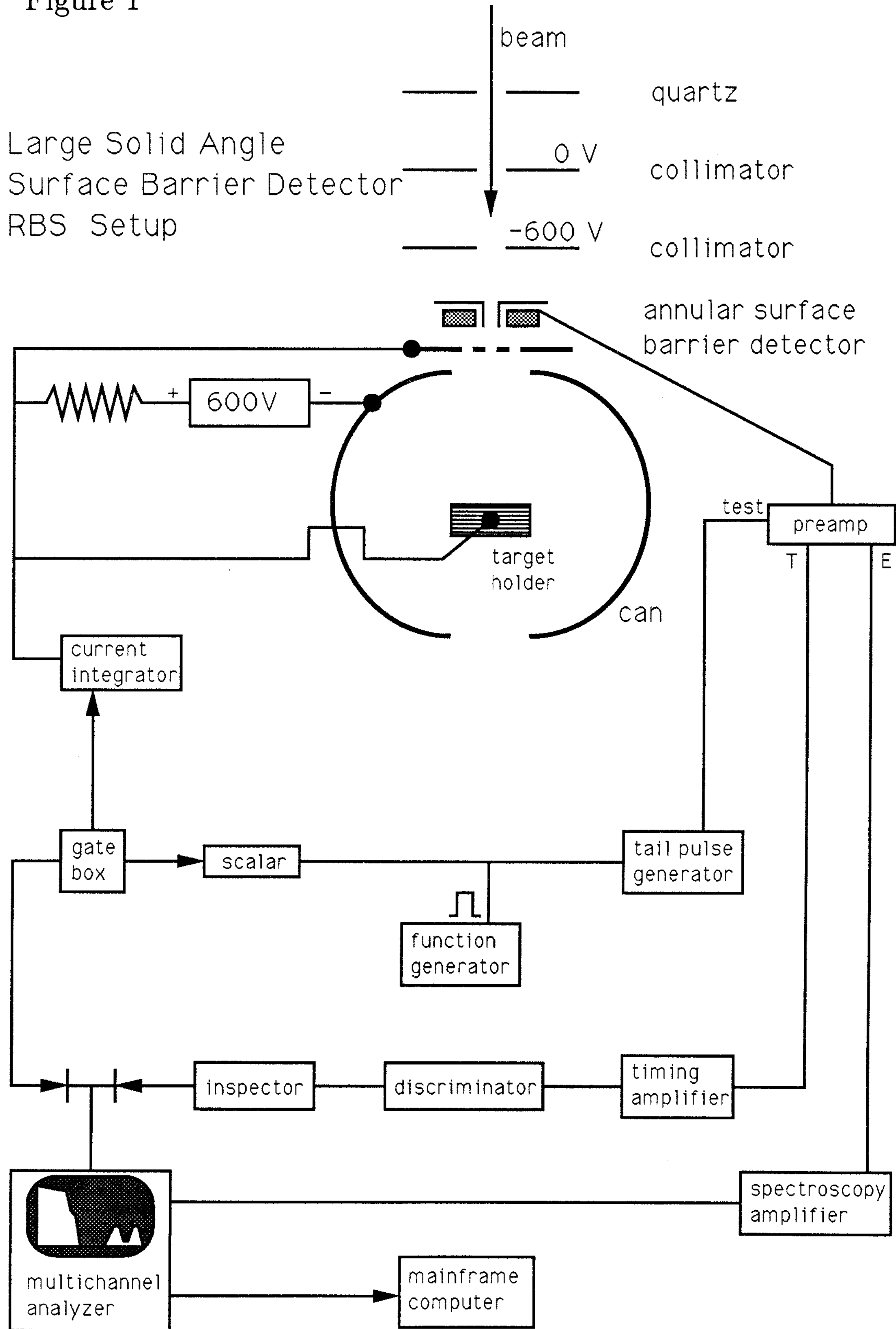

Figure 2

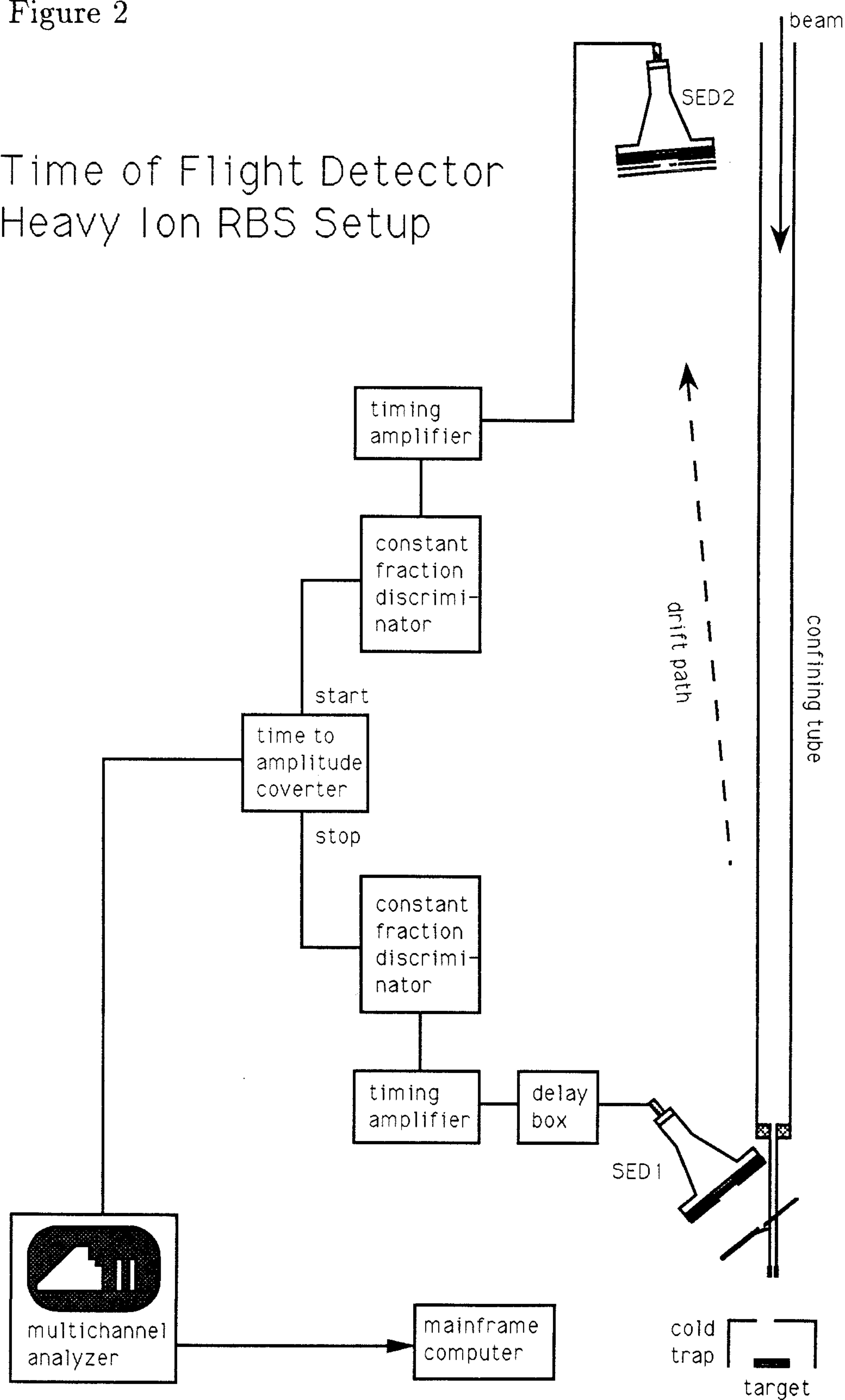

Figure 3

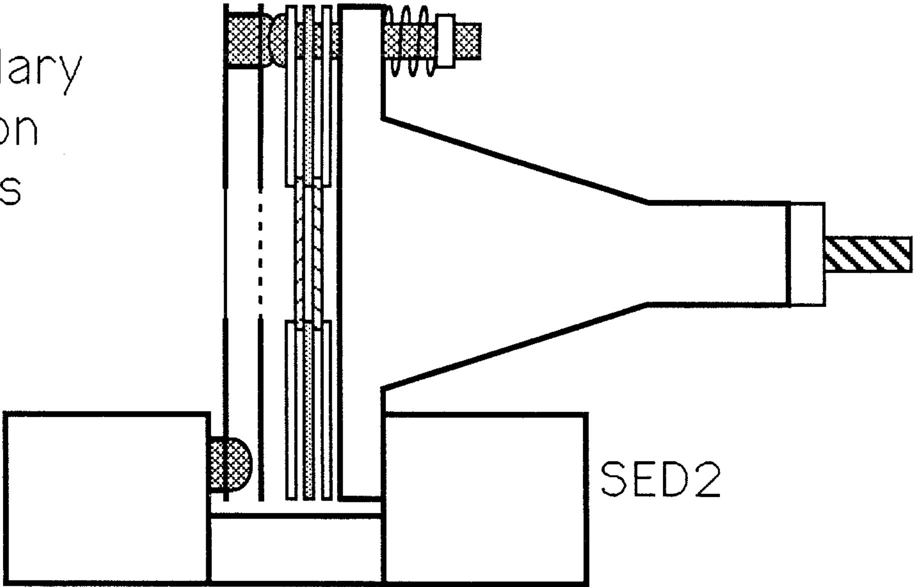

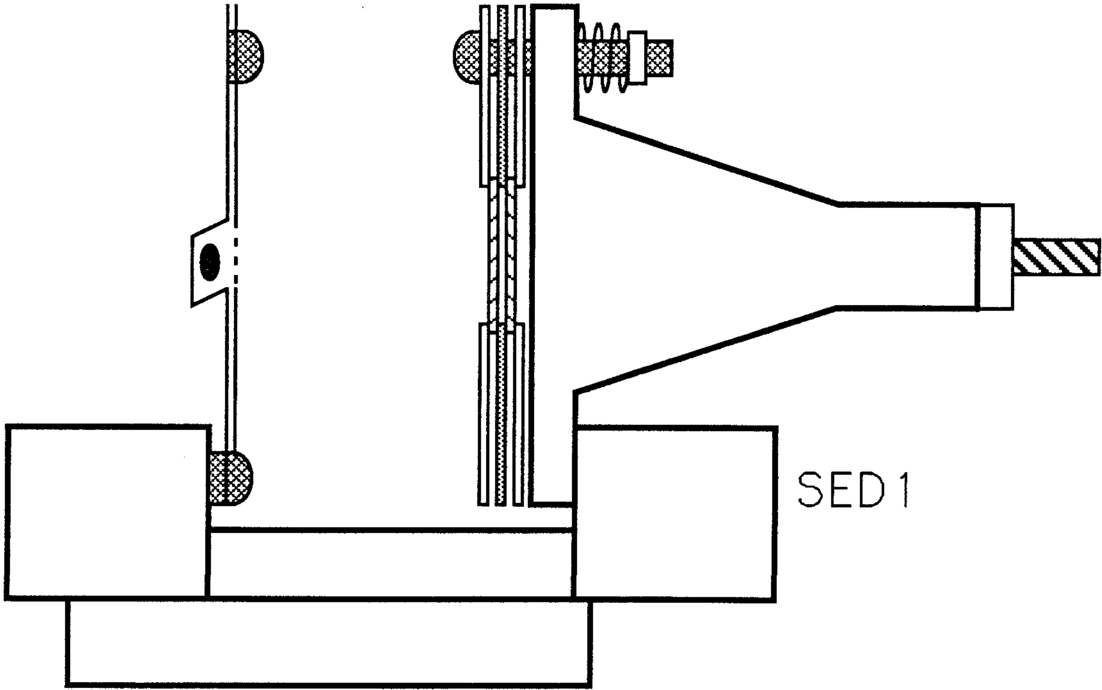

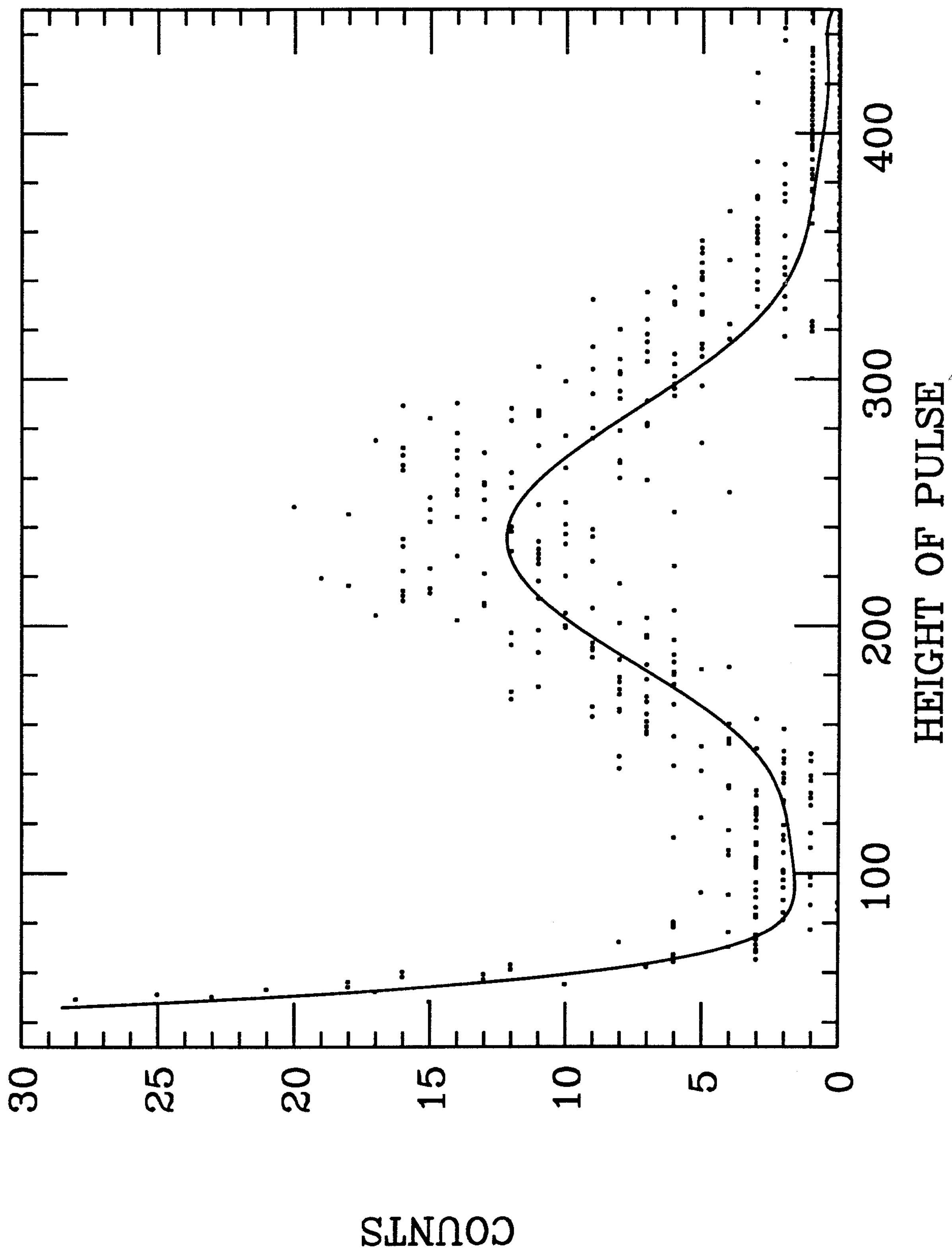
COUNTS
HEIGHT OF PULSE
0
5
10
15
20
25
30
100
200
300
400

Figure 5a

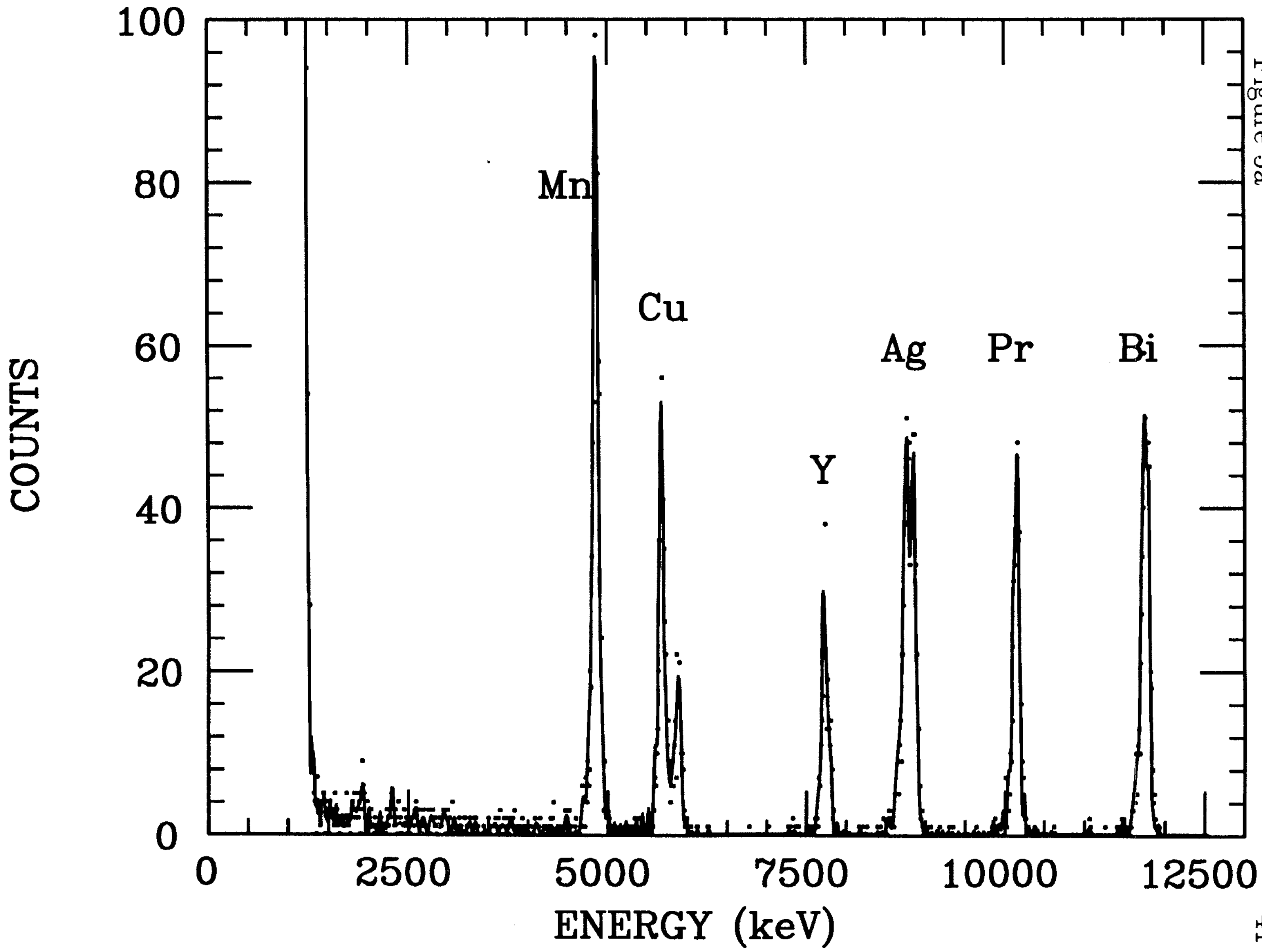

Figure 5b

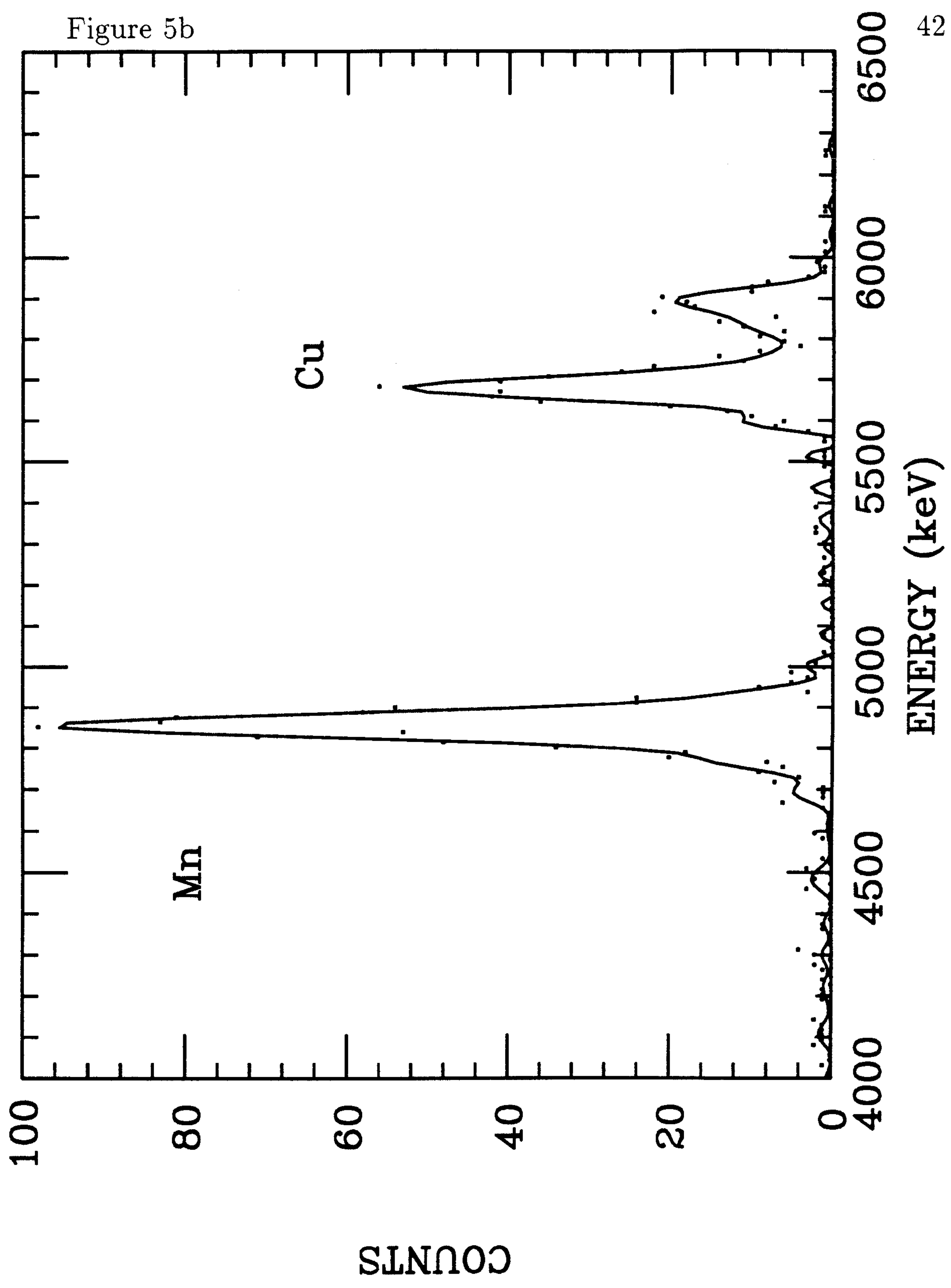

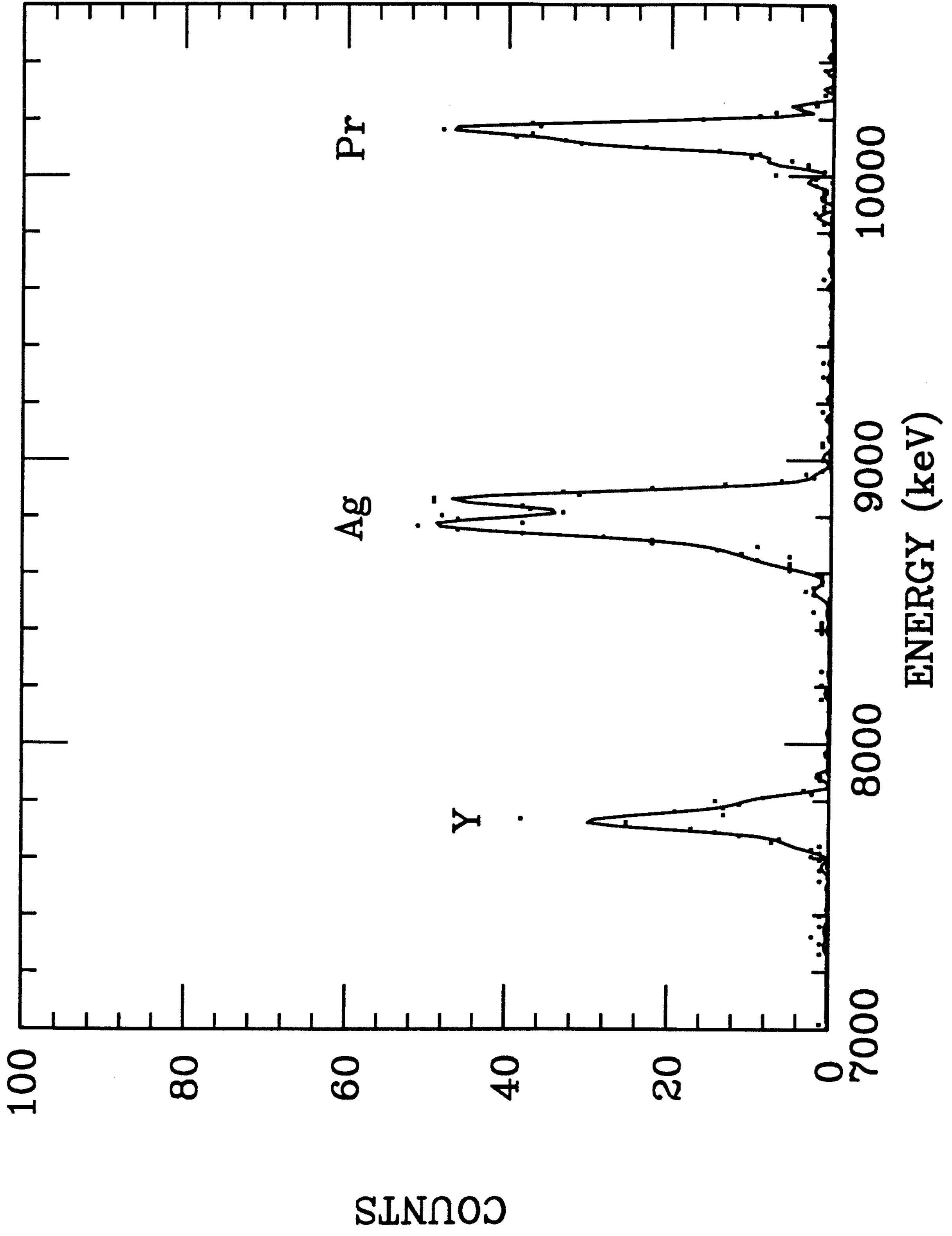
Pr
Ag
Y
COUNTS
ENERGY (keV)
0
20
40
60
80
100
7000
8000
9000
10000

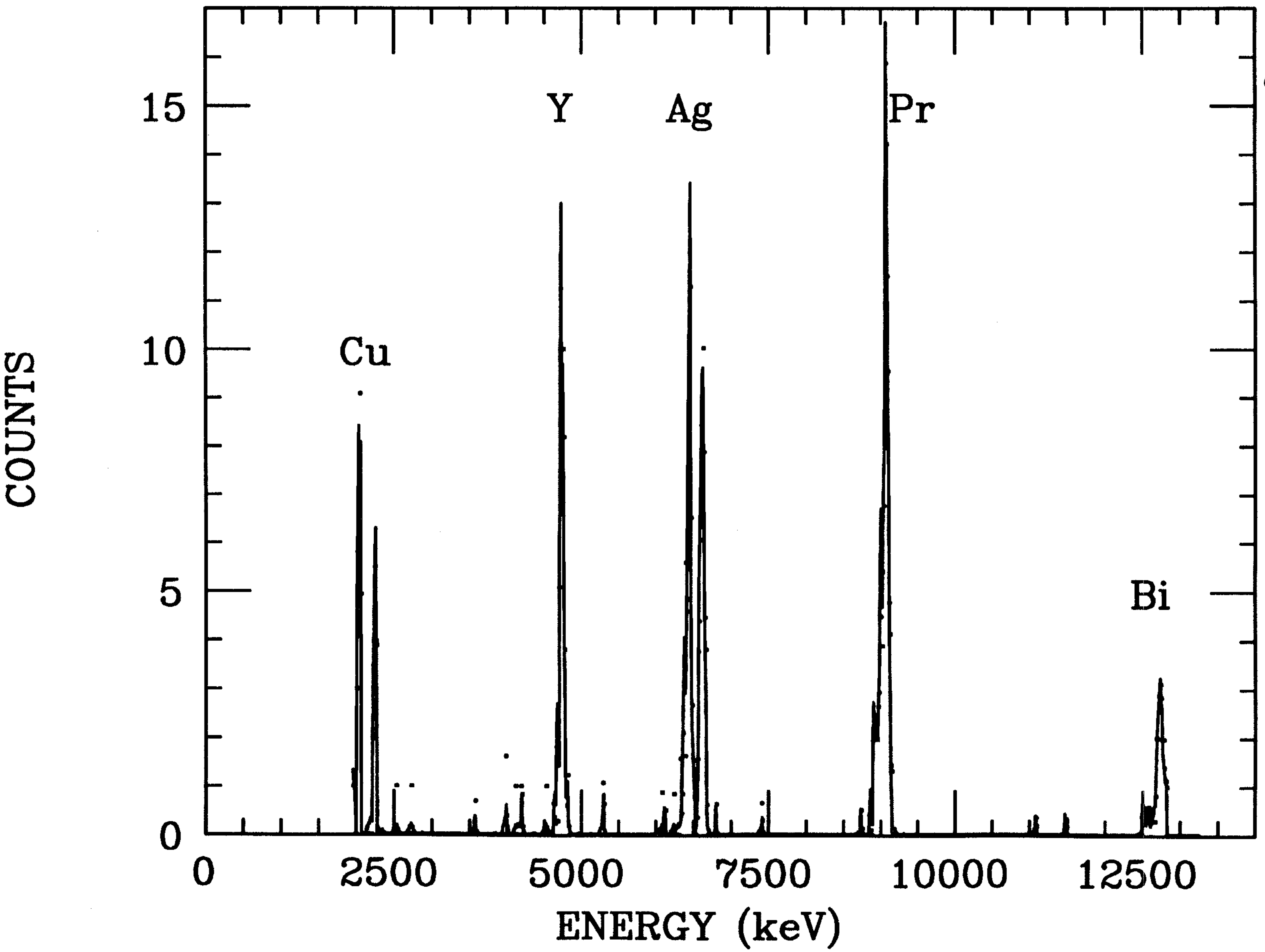
Cu
Y
Ag
Pr
Bi
COUNTS
0
5
10
15
0
2500
5000
7500
10000
12500
ENERGY (keV)

Figure 6b

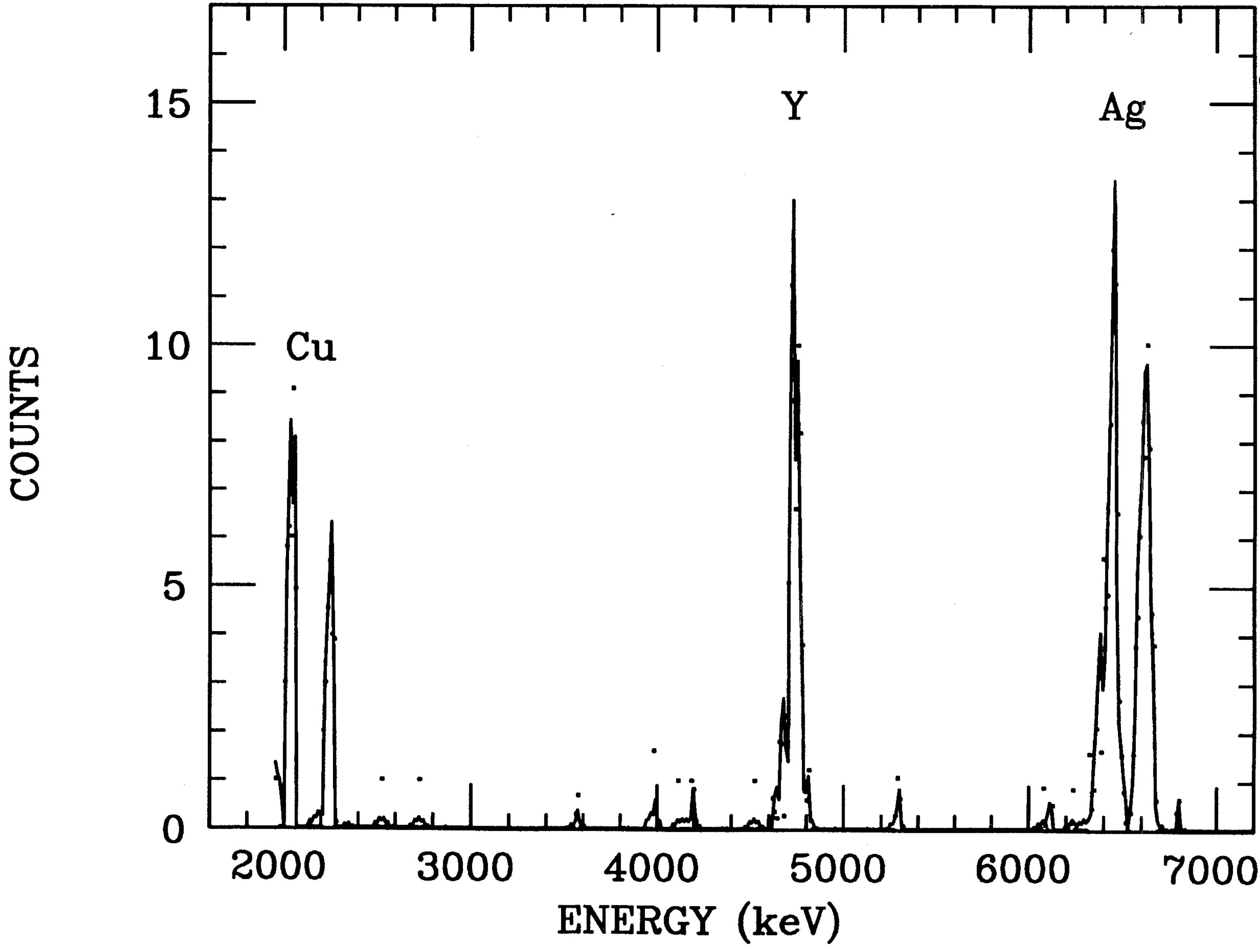

Figure 7a

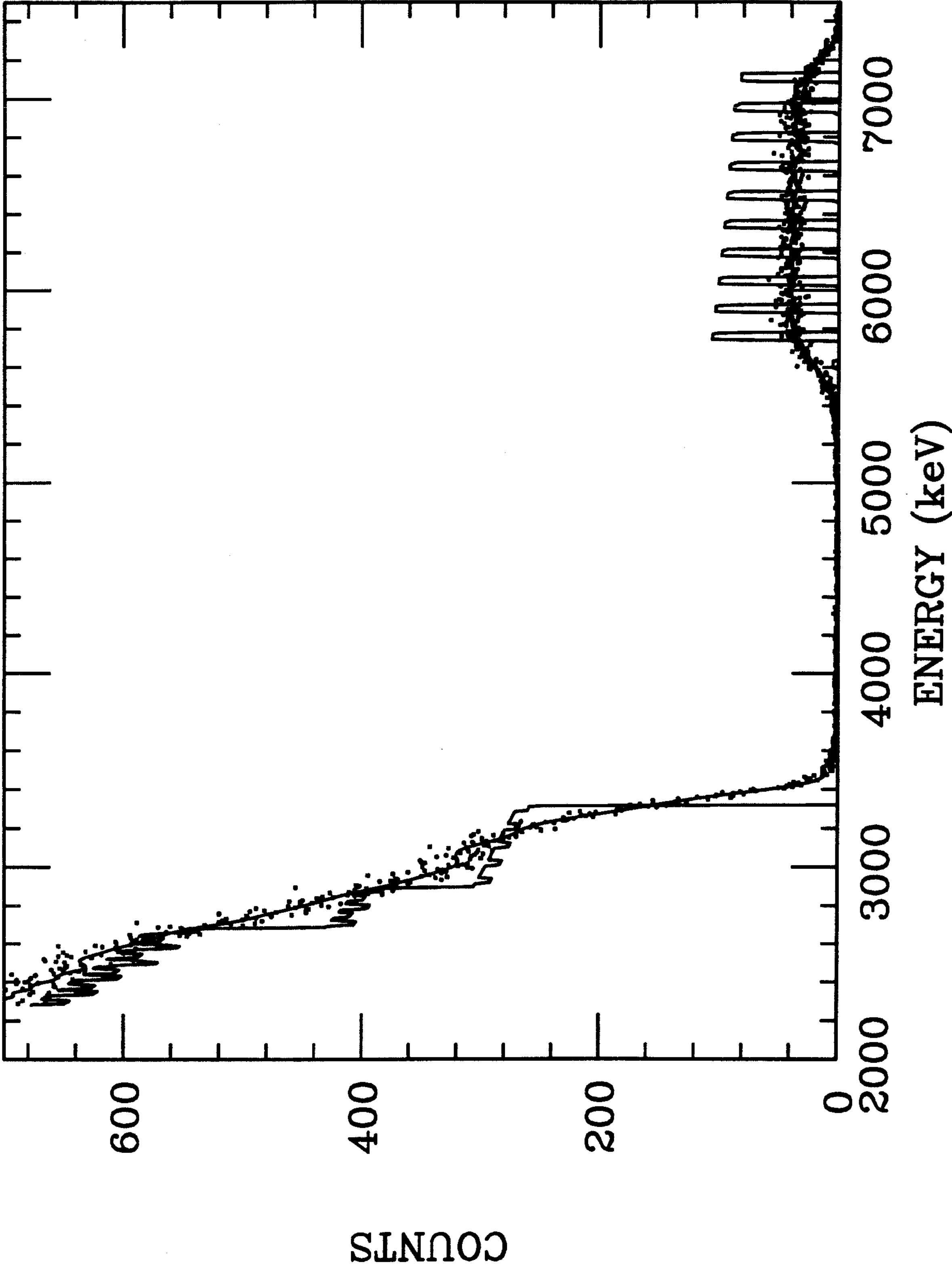

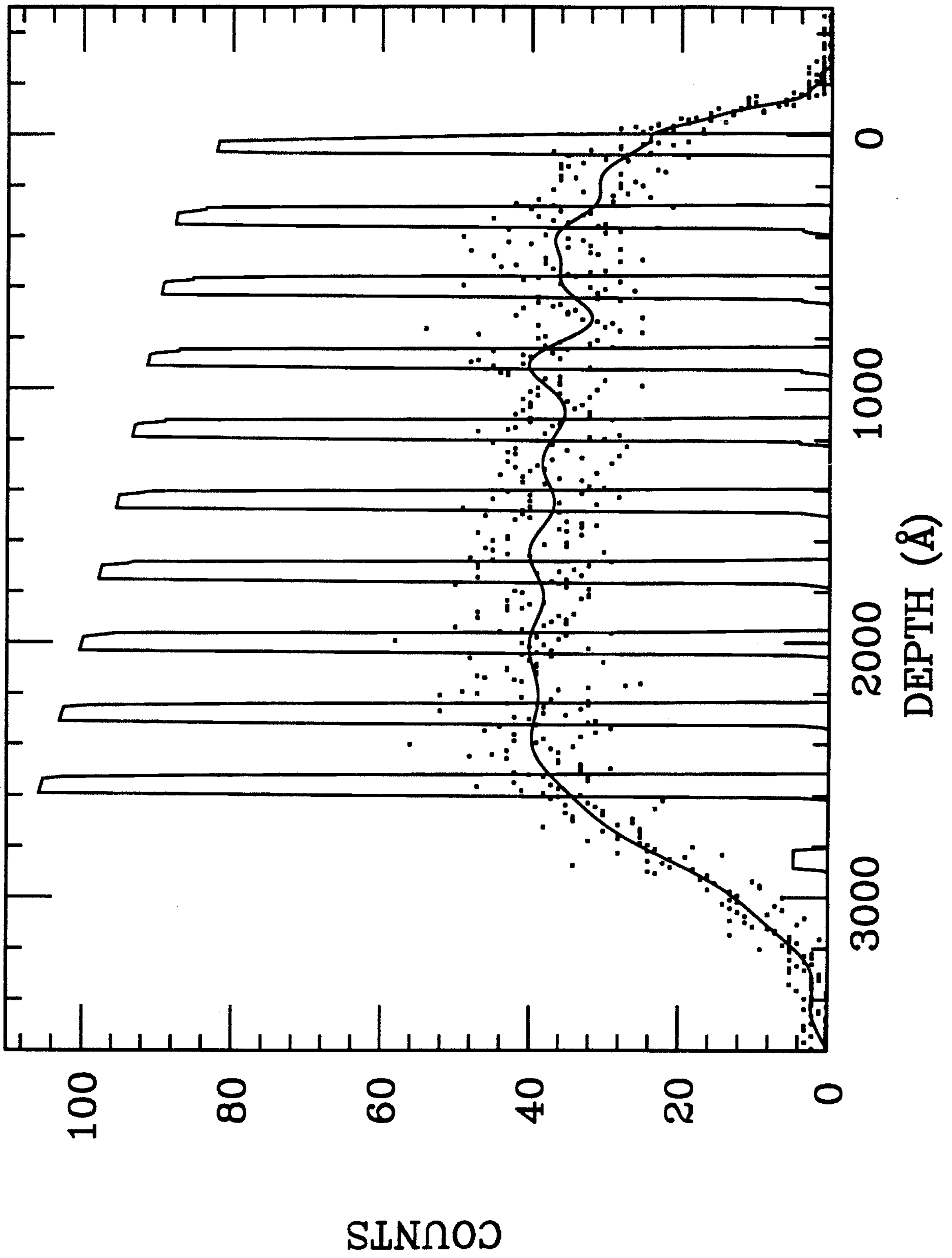
COUNTS
0
20
40
60
80
100
DEPTH (Å)
0
1000
2000
3000

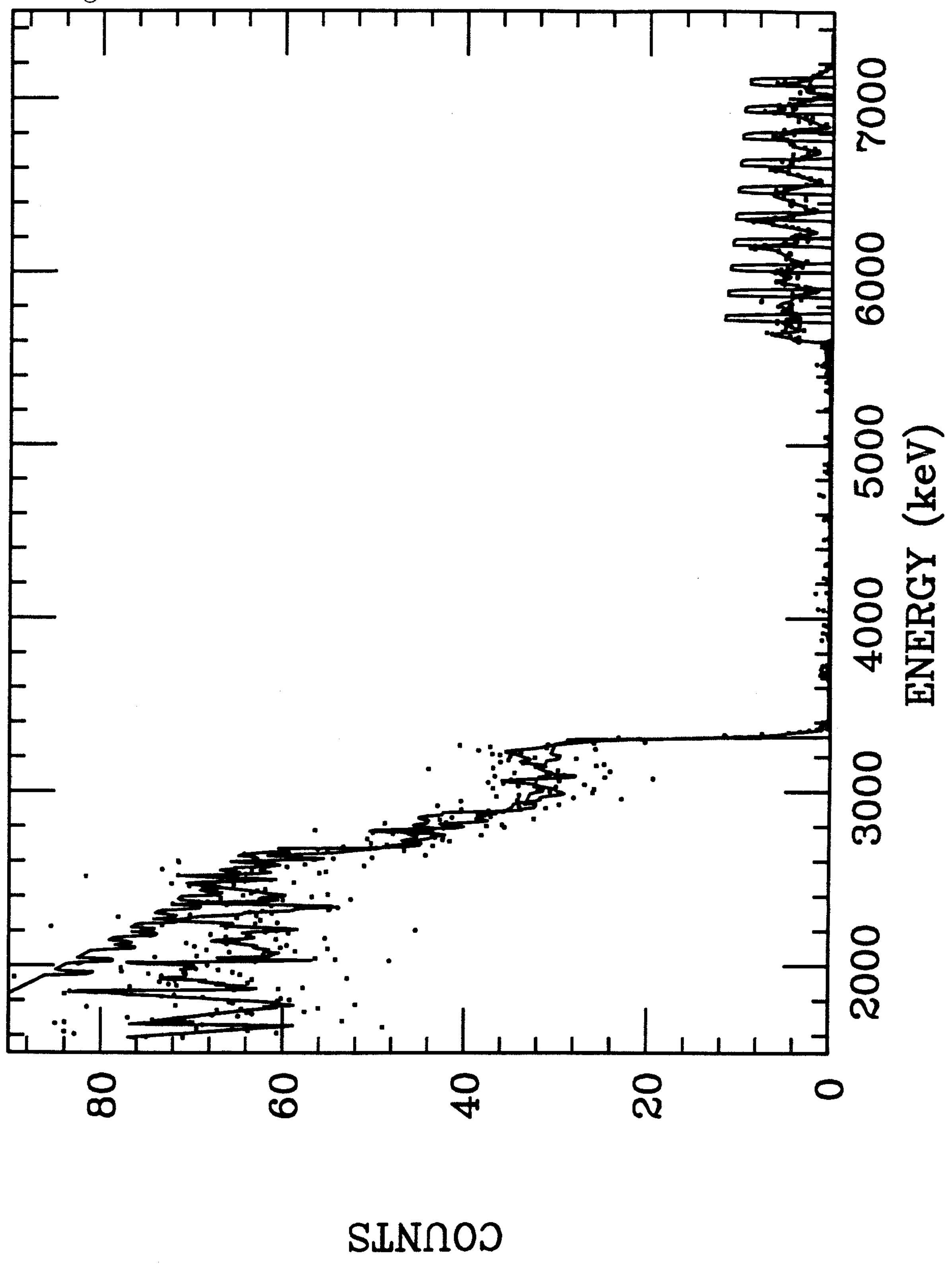
COUNTS
0
20
40
60
80
ENERGY (keV)
2000
3000
4000
5000
6000
7000

Figure 8b

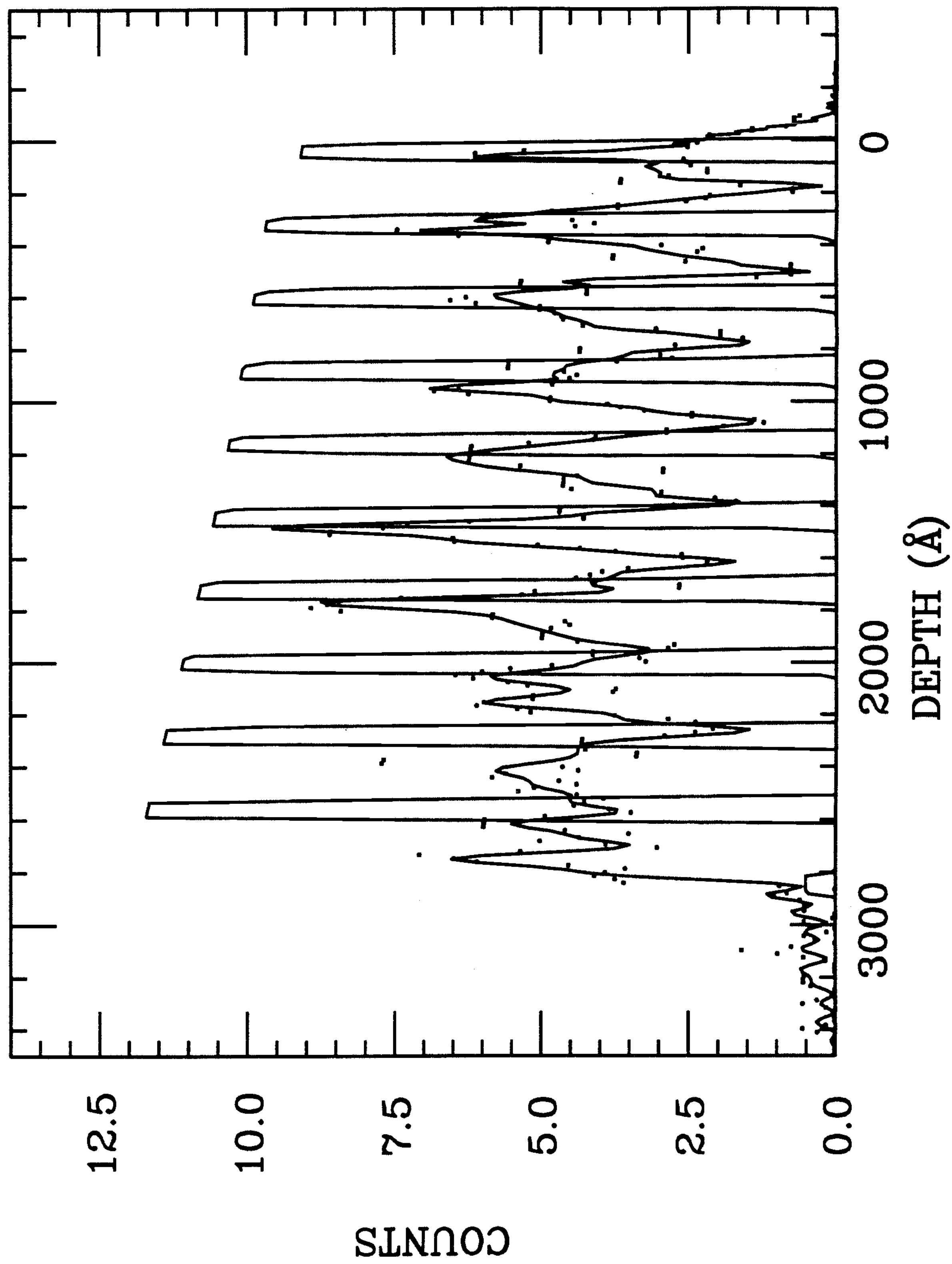

Figure 9a

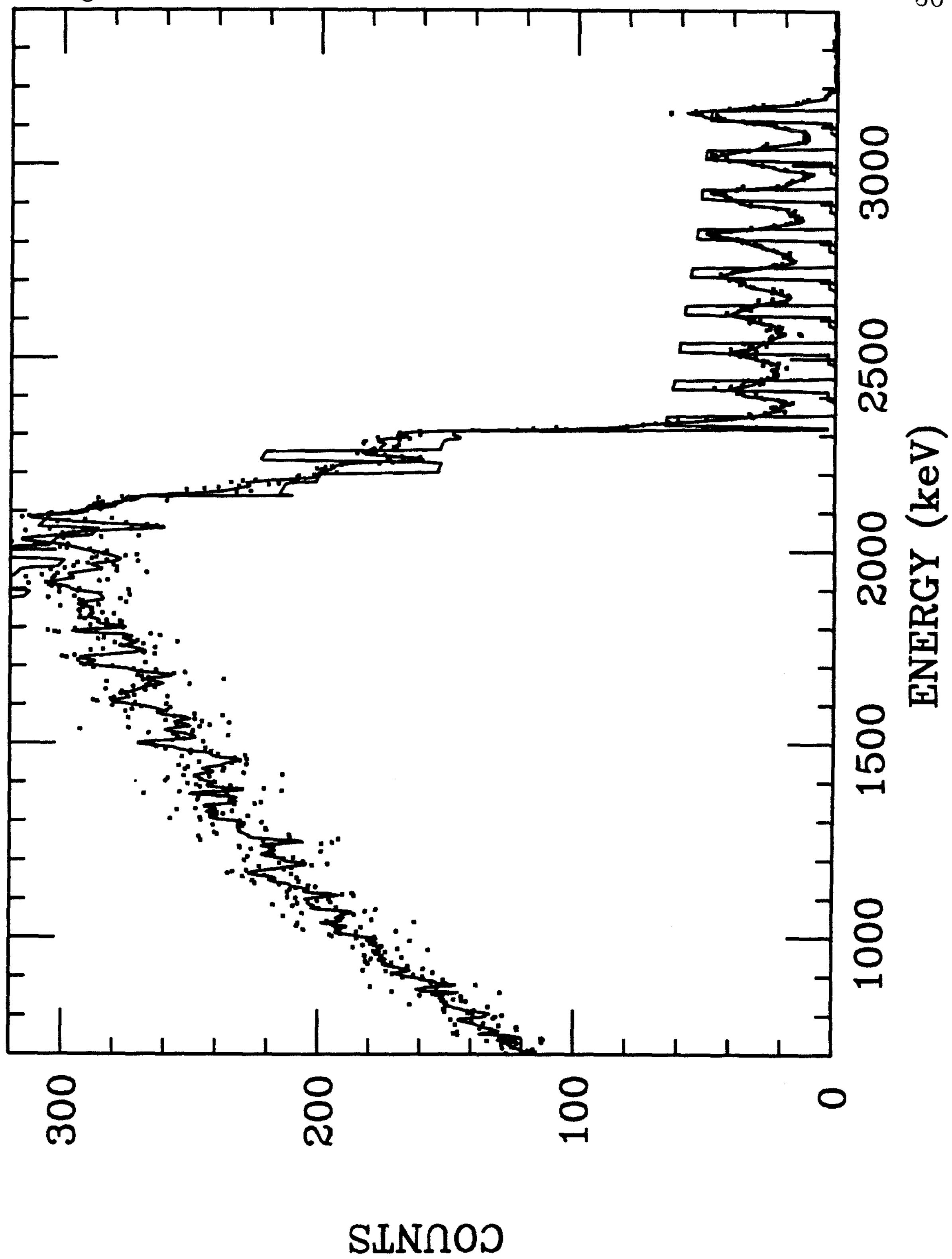

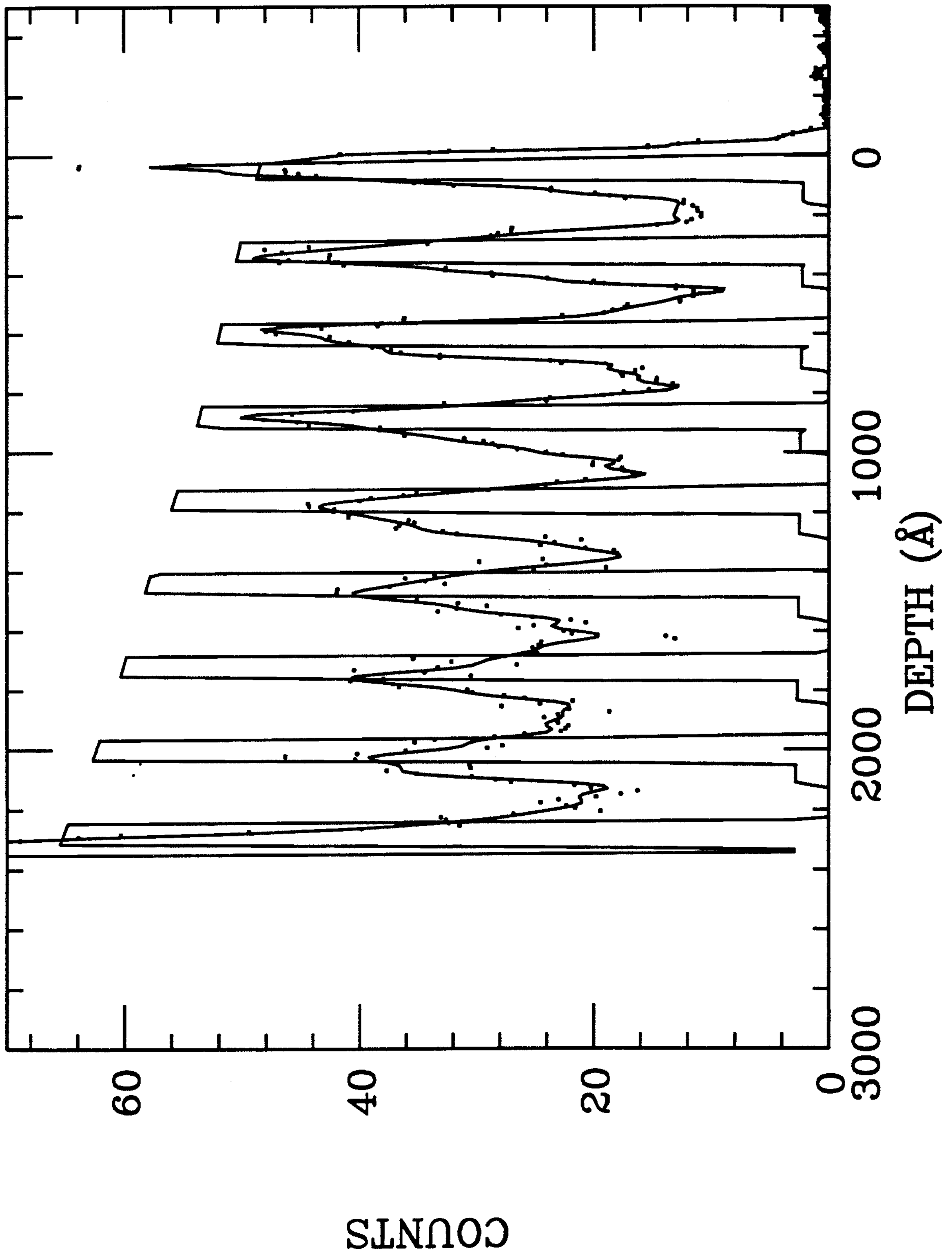
COUNTS
0
20
40
60
DEPTH (Å)
0
1000
2000
3000

Figure 10

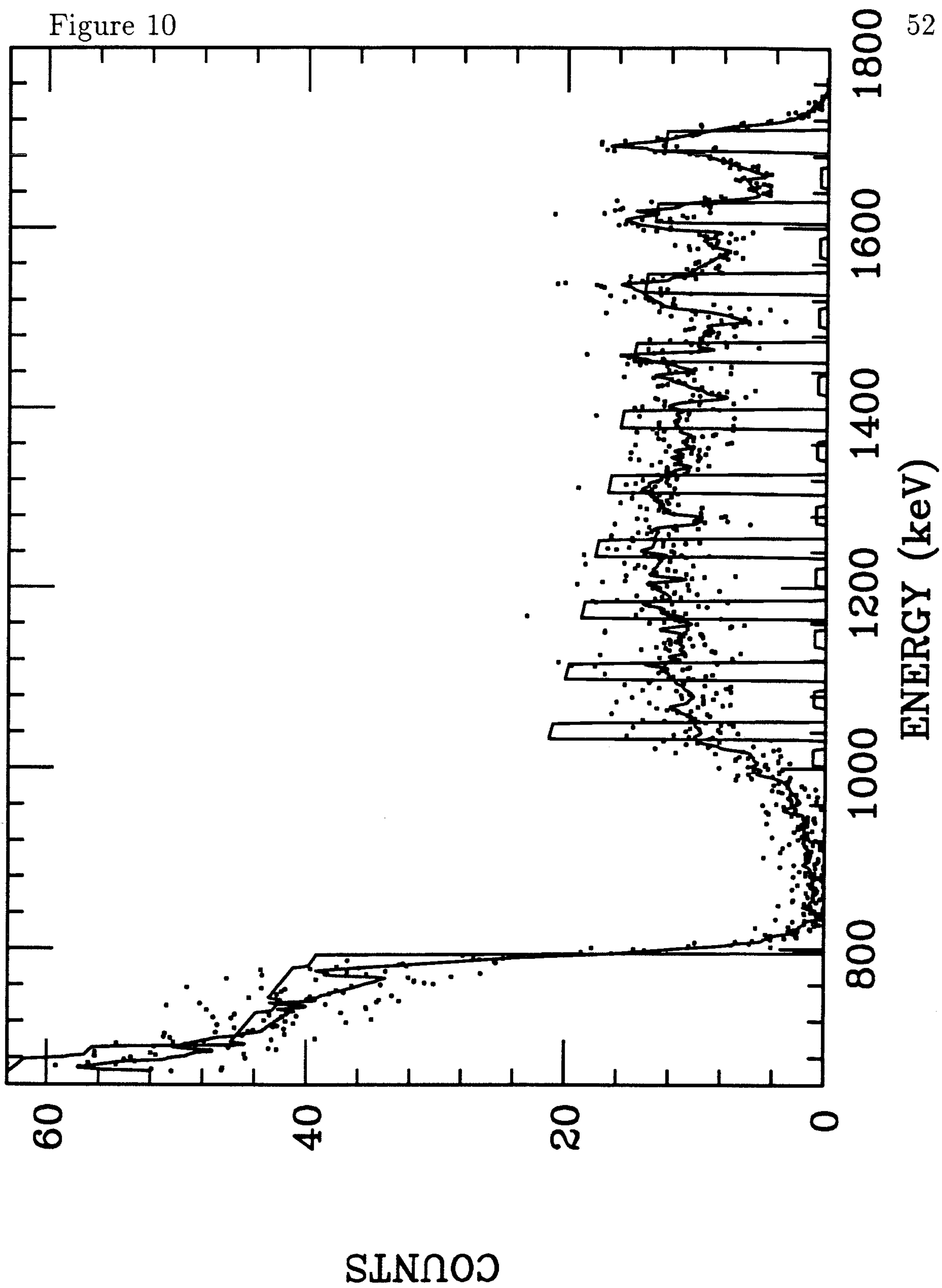

Figure 11

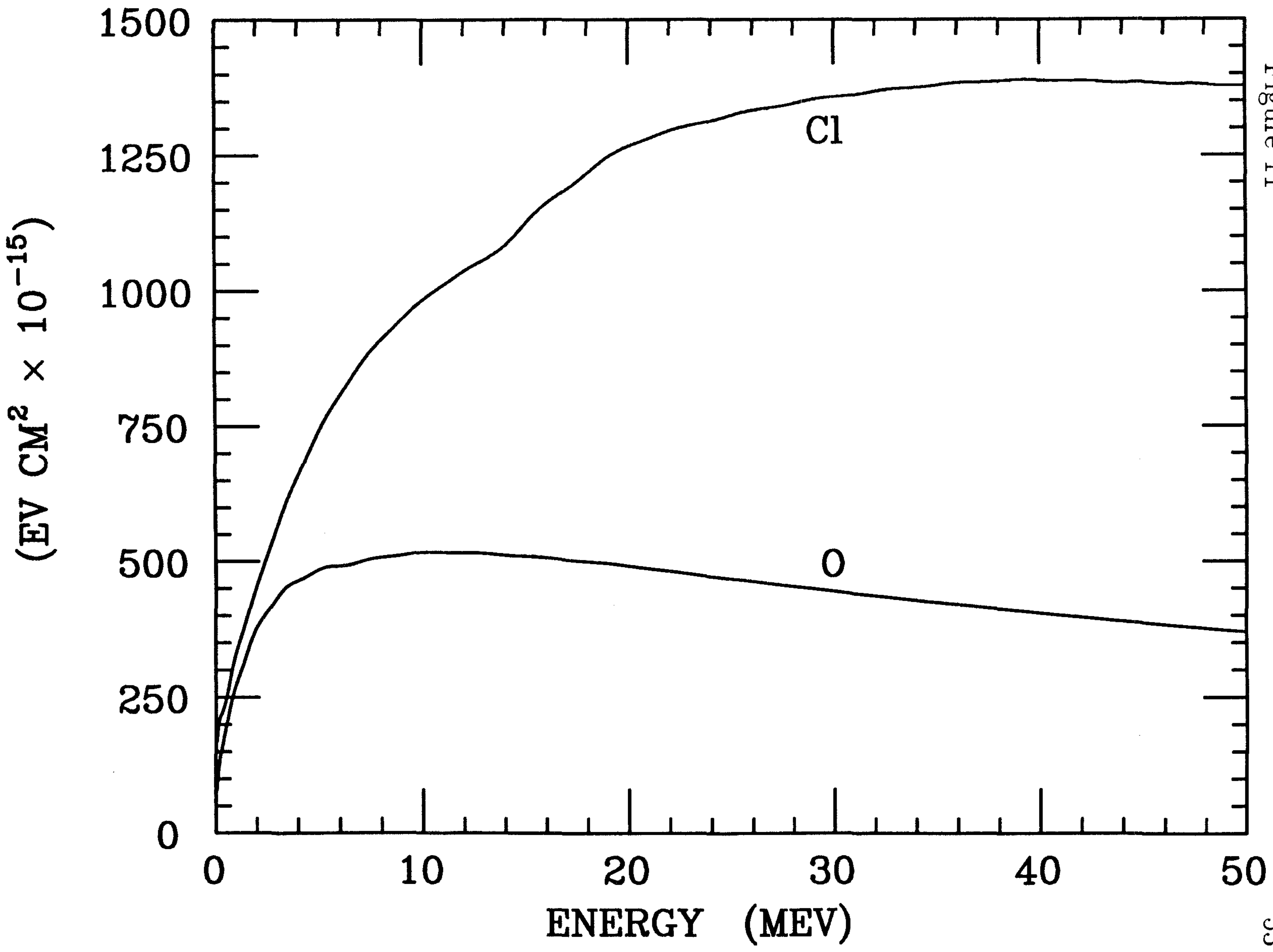

	surface		x=2600Å						
	ε_{in}	ε_{out}	ε_{in}	ε_{out}	$\frac{\Delta e}{\Delta x}$	Δe_l	κ	δt	χ_r^2
	$\frac{keV}{\AA}$		$\frac{keV}{\AA}$		$\frac{keV}{\AA}$	keV	$\frac{keV}{\sqrt{\mu m}}$	ps	
5.5 MeV O	.22	.19	.22	.18	.311	87	38	429	.016
25 MeV Cl	.585	.387	.576	.387	.554	155	59	270	.088
6 MeV Cl	.352	.187	.341	.165	.286	80	38	1593	.085

Results of analysis of Multilayer Heterojunction, as described in the text, for the three cases as shown in figures 8, 9, and 10. The first four columns are stopping powers before and after scattering, at the surface and at depth. The column labeled $\frac{\Delta e}{\Delta x}$ gives the energy separation as seen in the detector per Å of target depth. Δe_l is the energy separation of the layers. κ is the fitted value of the straggling parameter, δt that of the time resolution, and χ_r^2 gives an indication of the goodness of fit.

	layer	δe	δe_{fit}	$\frac{de}{dt}$	$\kappa\sqrt{x}$	δx
		keV	keV	$\frac{kev}{ns}$	kev	$\AA$
5.5 MeV O	1	20.0	19.6	45.1	3.4	63
	2	20.4	20.5	42.9	9.1	66
	3	20.9	21.5	40.8	12.4	69
	4	20.1	22.5	38.7	15.2	72
	5	24.2	23.8	36.5	17.9	77
	6	25.7	24.9	34.6	20.0	80
	7	26.6	26.1	32.8	22.0	84
	8	26.6	27.4	30.9	24.0	88
25 MeV Cl	1	28.5	29.1	106.5	4.9	53
	2	30.0	30.9	103.2	13.6	56
	3	35.0	32.7	100.0	18.5	59
	4	36.9	35.1	95.8	23.7	63
	5	38.1	36.9	92.5	27.3	67
	6	35.7	38.8	89.4	30.4	70
	7	39.5	40.7	86.1	33.5	73
	8	42.9	43.2	82.1	37.2	78
	9	44.8	45.1	79.1	39.8	81
	10	48.9	46.9	76.3	42.2	85
6 MeV Cl	1	20.0	20.1	12.4	3.6	70
	2	22.0	21.5	11.5	11.2	75
	3	23.0	23.1	10.7	15.5	81
	4	23.0	24.7	10.0	18.8	86
	5	28.6	26.3	9.3	21.7	92
	6	27.2	27.9	8.7	24.1	98

Results of analysis of Multilayer Heterojunction, giving resolutions by layer. For each analyzable layer the total energy resolution is given. $\frac{de}{dt}$ is the timing resolution contribution to the energy resolution; $\kappa\sqrt{x}$ is the contribution from straggling. δx is the depth resolution.

Figure 14

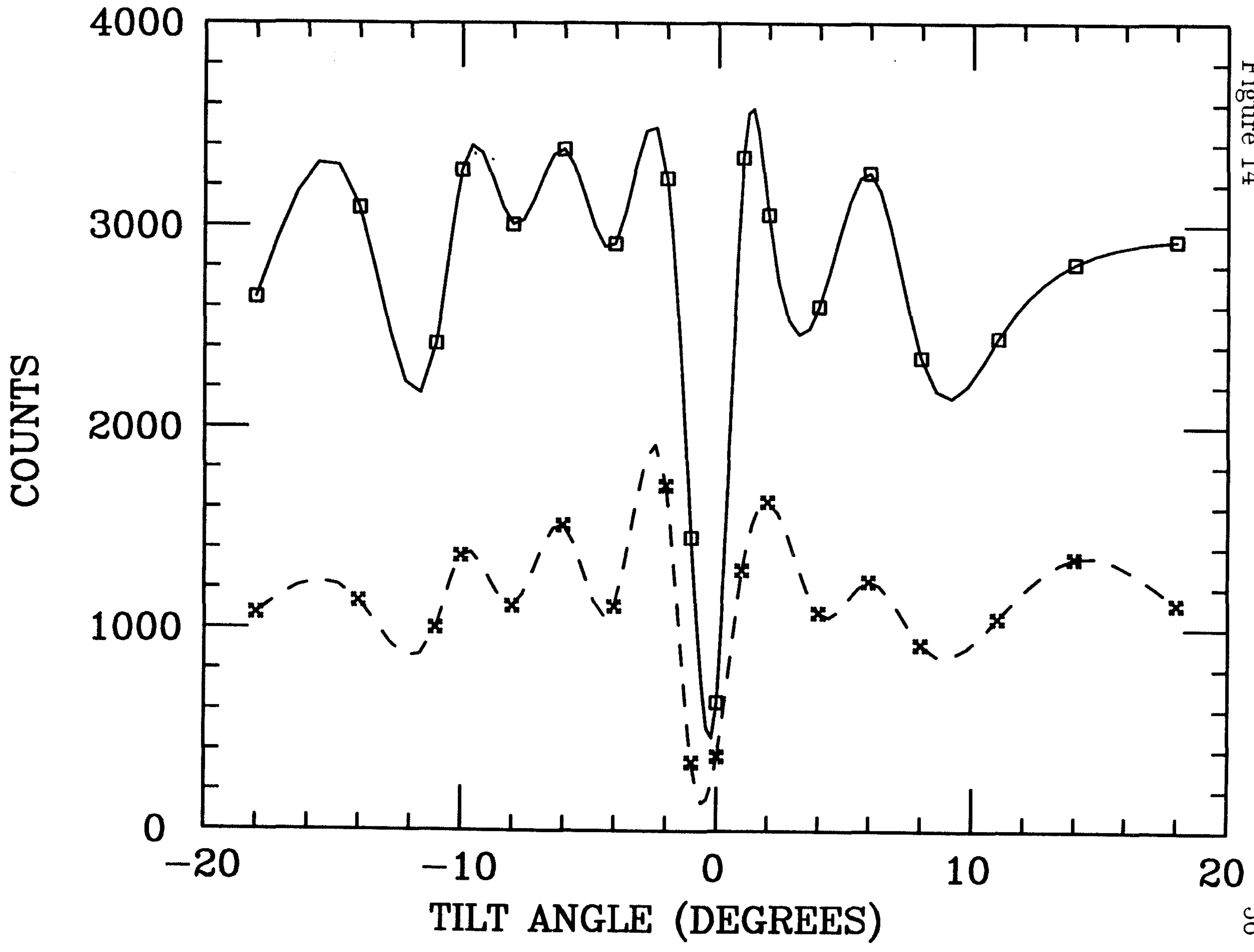

sample	x fab	x exp	d fab	d exp	2f fab	2f exp	a fab	a exp
	Å		Å				$\times 10^{15} \frac{atoms}{cm^2}$	
3881	100	408	0		.1	.084	2.17	7.11
3885	200	301	0		.1	.097	4.34	6.09
3882	300	223	0		.1	.058	6.52	2.47
3893	100	333	0		.15	.071	3.23	5.03
3901	200	477	0		.15	.038	6.45	3.51
3905	300	283	0		.15	.029	9.68	1.61
3887	100	112	0		.2	.14	4.26	3.26
3917	200	163	0		.2	.17	8.52	6.27
3921	300	320	0		.2	.16	12.79	11.12
3884	100	196	300	243	.1	.048	2.17	2.02
3886	200	259	300	291	.1	.041	4.34	2.33
3883	300	290	300	273	.1	.11	6.52	7.15
3894	100	184	300	210	.15	.056	3.23	2.59
3902	200	230	300	264	.15	.094	6.45	4.79
3914	300	331	300	271	.15	.12	9.68	8.57
3890	100	141	300	195	.2	.087	4.26	3.90
3919	200	194	300	193	.2	.14	8.52	7.29
3920	300	329	300	293	.2	.14	12.79	9.99

Results of the $In_xGa_{1-x}As$ quantum well analysis with a surface barrier detector. The samples were epitaxial $In_xGa_{1-x}As$ on $GaAs$ with an optional layer of $GaAs$ above. *fab* is the intended (fabricated) value, *exp* the experimental one. x is the thickness of the $In_xGa_{1-x}As$ layer, d the depth of the layer beneath the surface, *2f* is the same as x in the formula $In_xGa_{1-x}As$, and a is the total amount of In.

sample	x fab	x exp	d fab	d exp	2f fab	2f exp	C on surface
	Å		Å				Å
3881	100	290	0		.1	.15	65
3885	200	180	0	20	.1	.25	25
3882	300	100	0	15	.1	.2	25
3893	100	280	0		.15	.15	55
3901	200	215	0	25	.15	.15	30
3905	300	125	0		.15	.2	25
3887	100	90	0		.2	.3	50
3917	200	200	0		.2	.2	50
3921	300	320	0	300	.2	.3	25
3884	100	150	300	240	.1	.25	65
3886	200	185	300	340	.1	.1	25
3883	300	350	300	310	.1	.15	25
3894	100	160	300	300	.15	.15	35
3902	200	180	300	320	.15	.2	50
3914	300	300	300	320	.15	.3	25
3890	100	320	300	350	.2	.2	25
3919	200	150	300	300	.2	.5	50
3920	300	250	300	320	.2	.3	25

Results of the $In_xGa_{1-x}As$ quantum well analysis using the ToF detector. The same information as in figure 15 is tabulated except that C is the calculated thickness of hydrocarbon buildup on the surface.

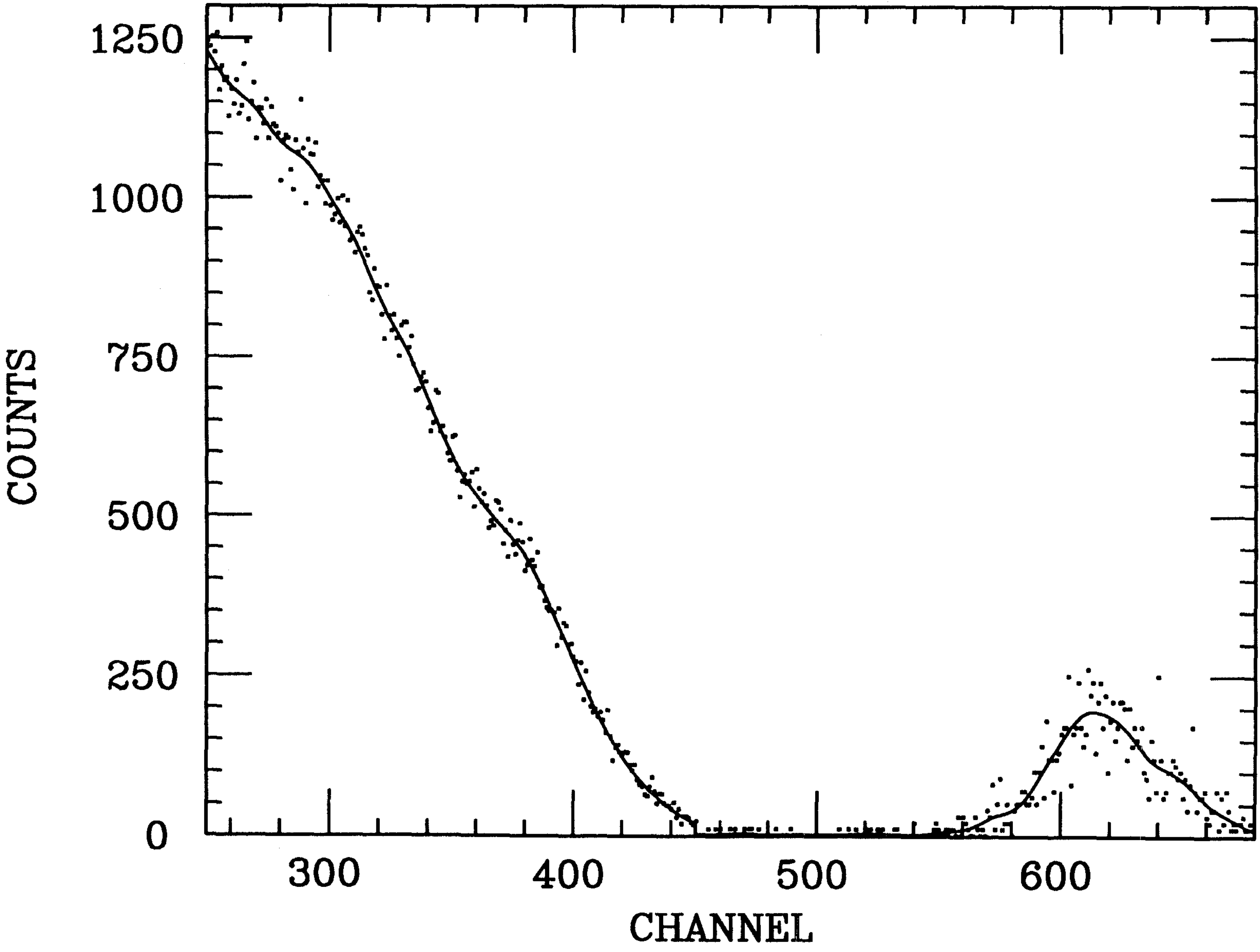

Figure 17a

Figure 17b

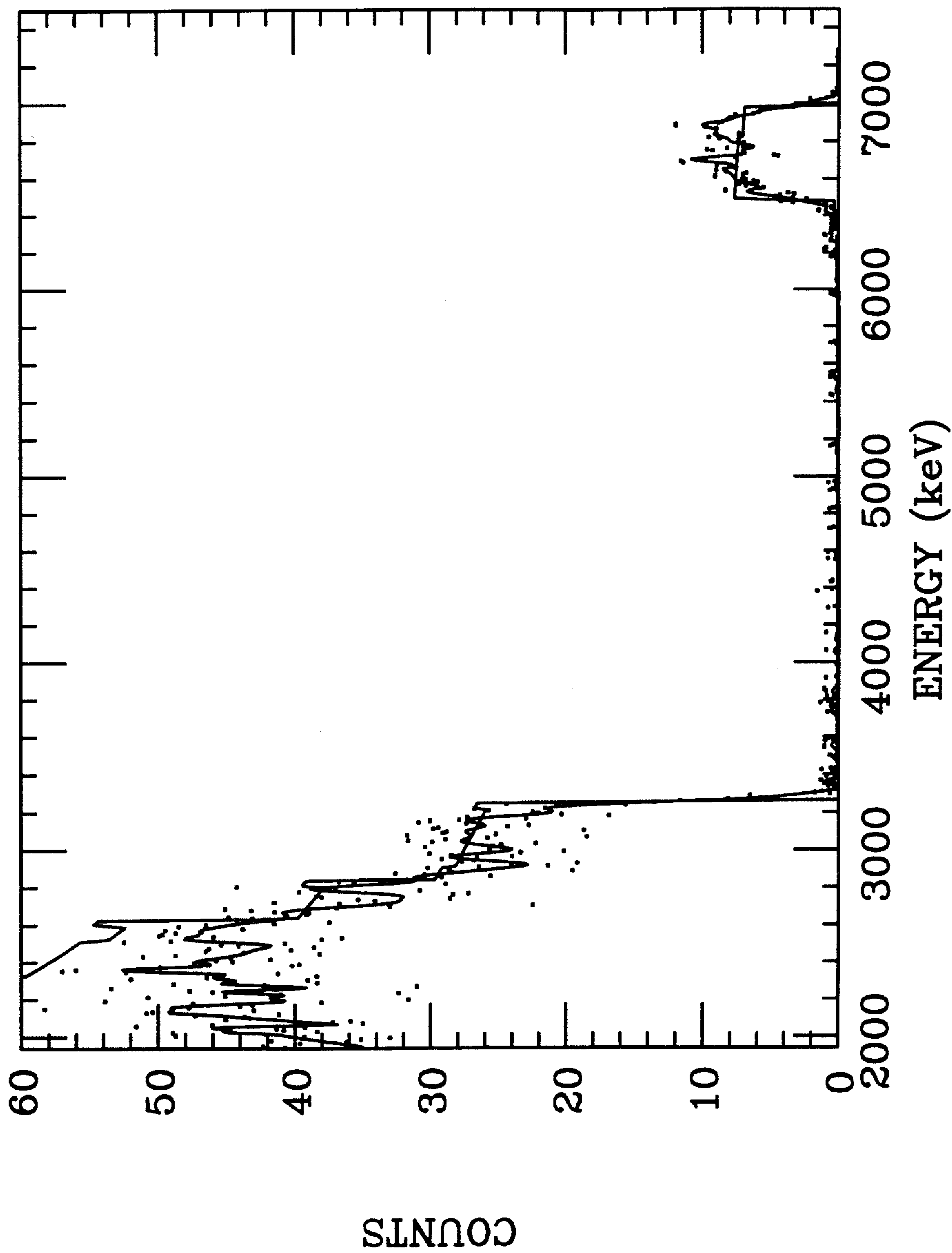

Figure 18a

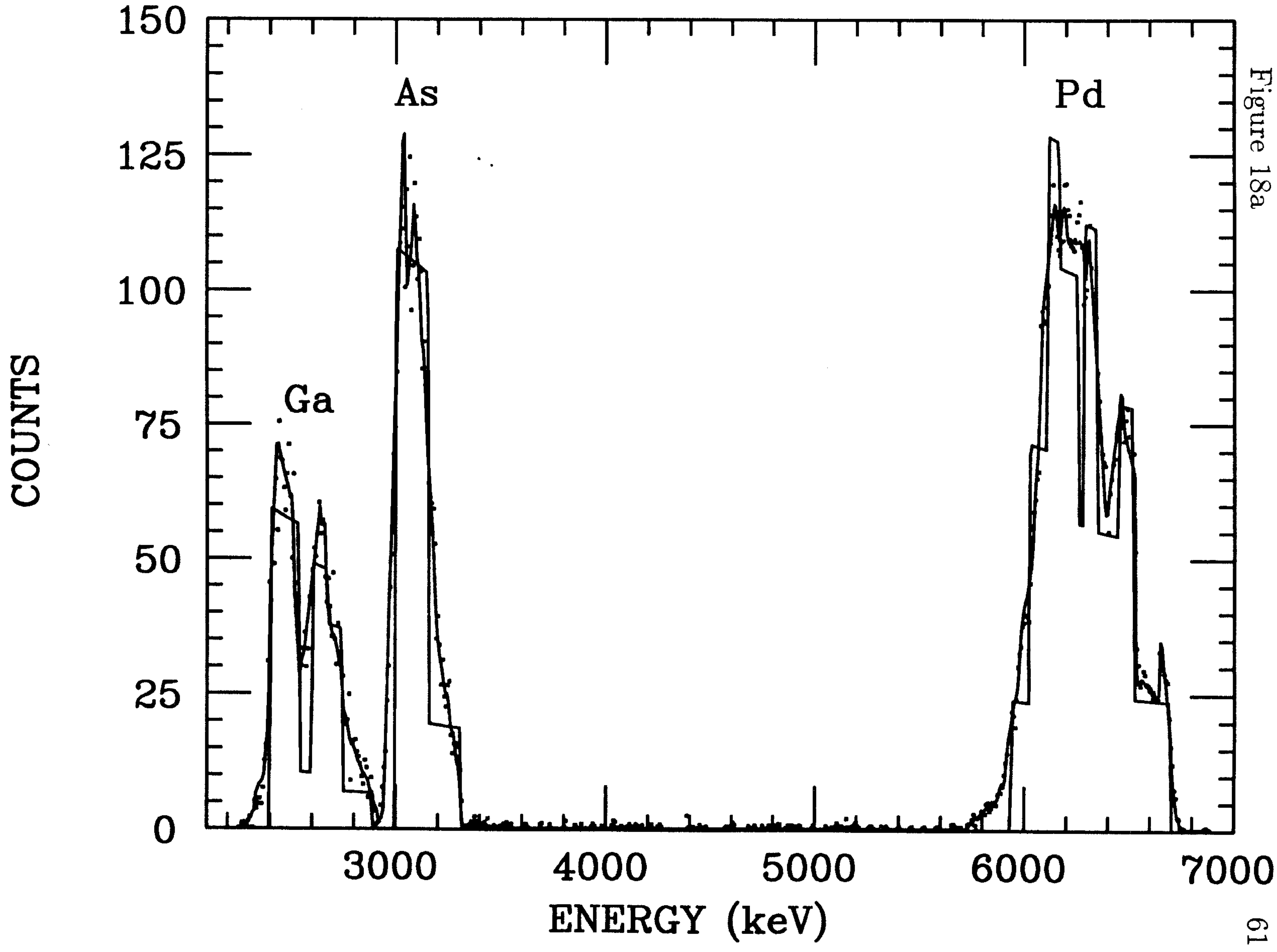

Figure 18b

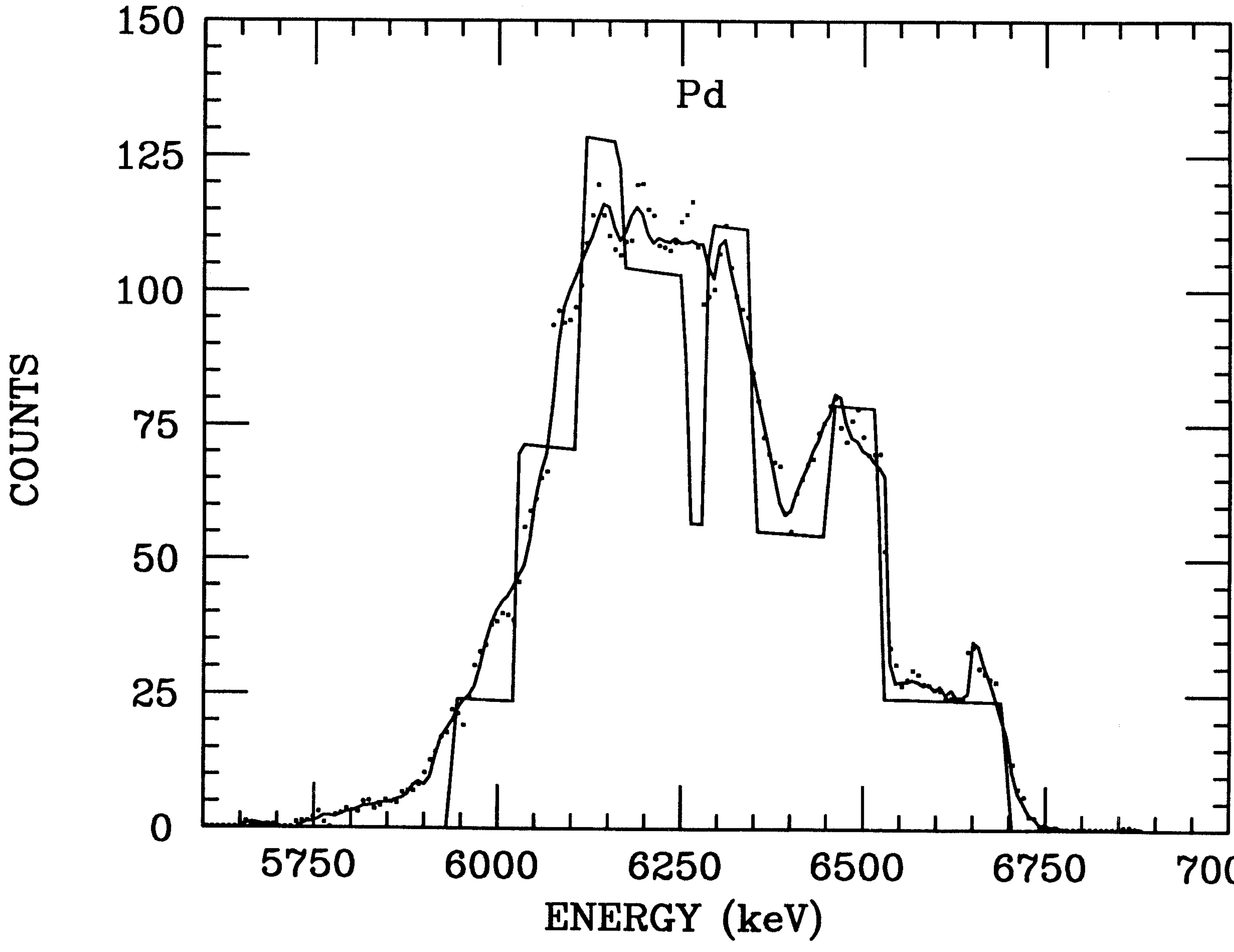

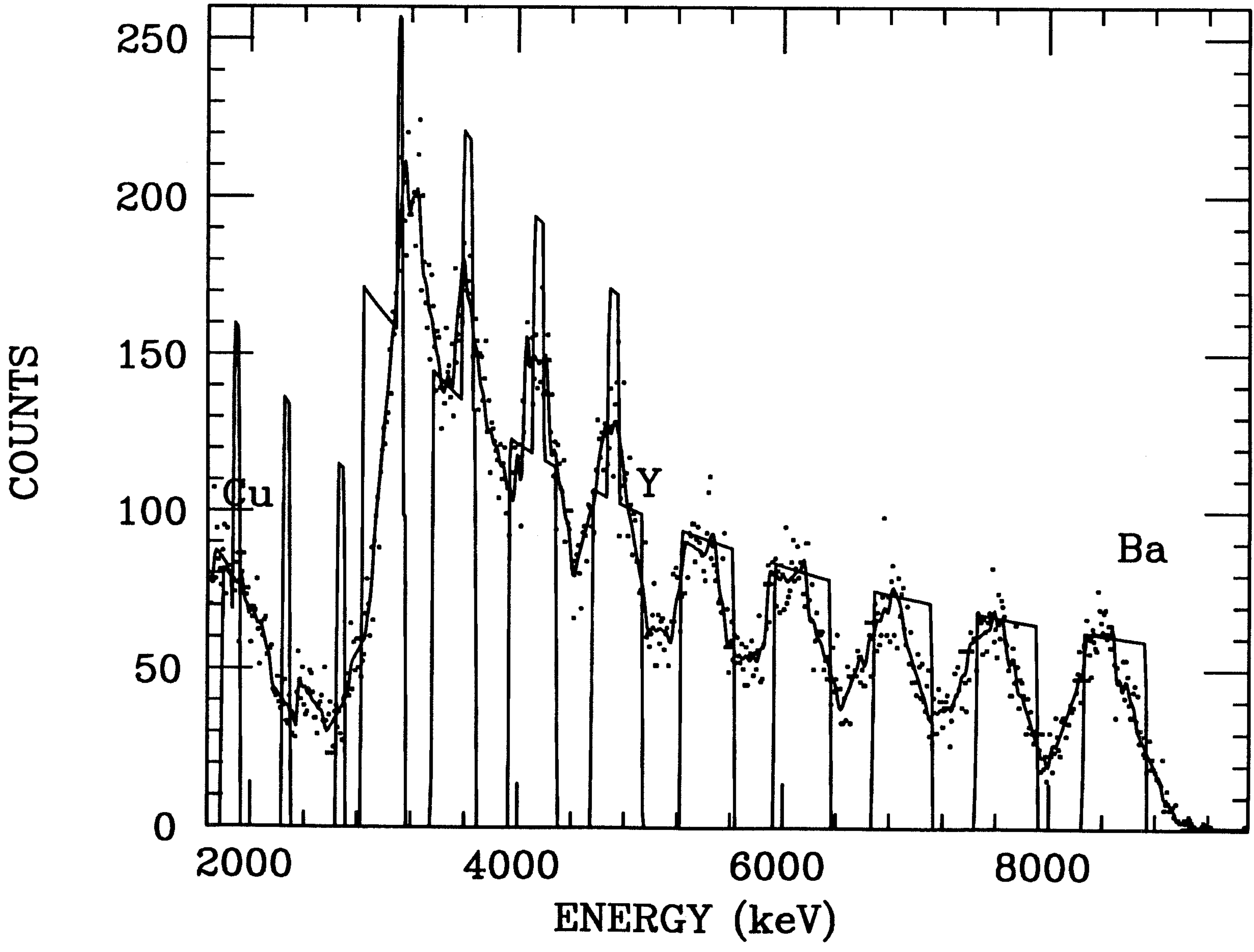
COUNTS
ENERGY (keV)
0
50
100
150
200
250
2000
4000
6000
8000
Cu
Y
Ba

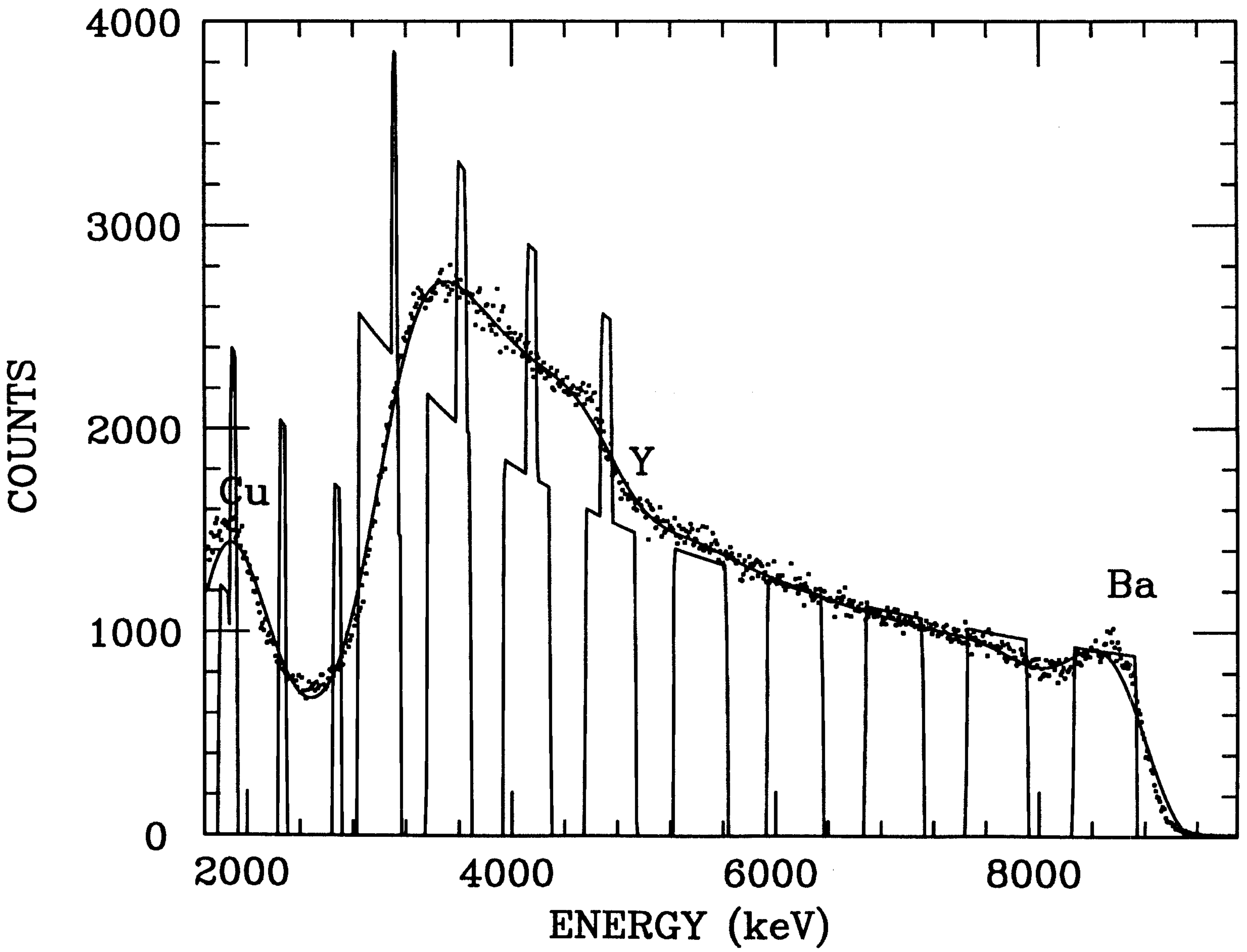
COUNTS
4000
3000
2000
1000
0
ENERGY (keV)
2000
4000
6000
8000
Cu
Y
Ba

Figure 21a

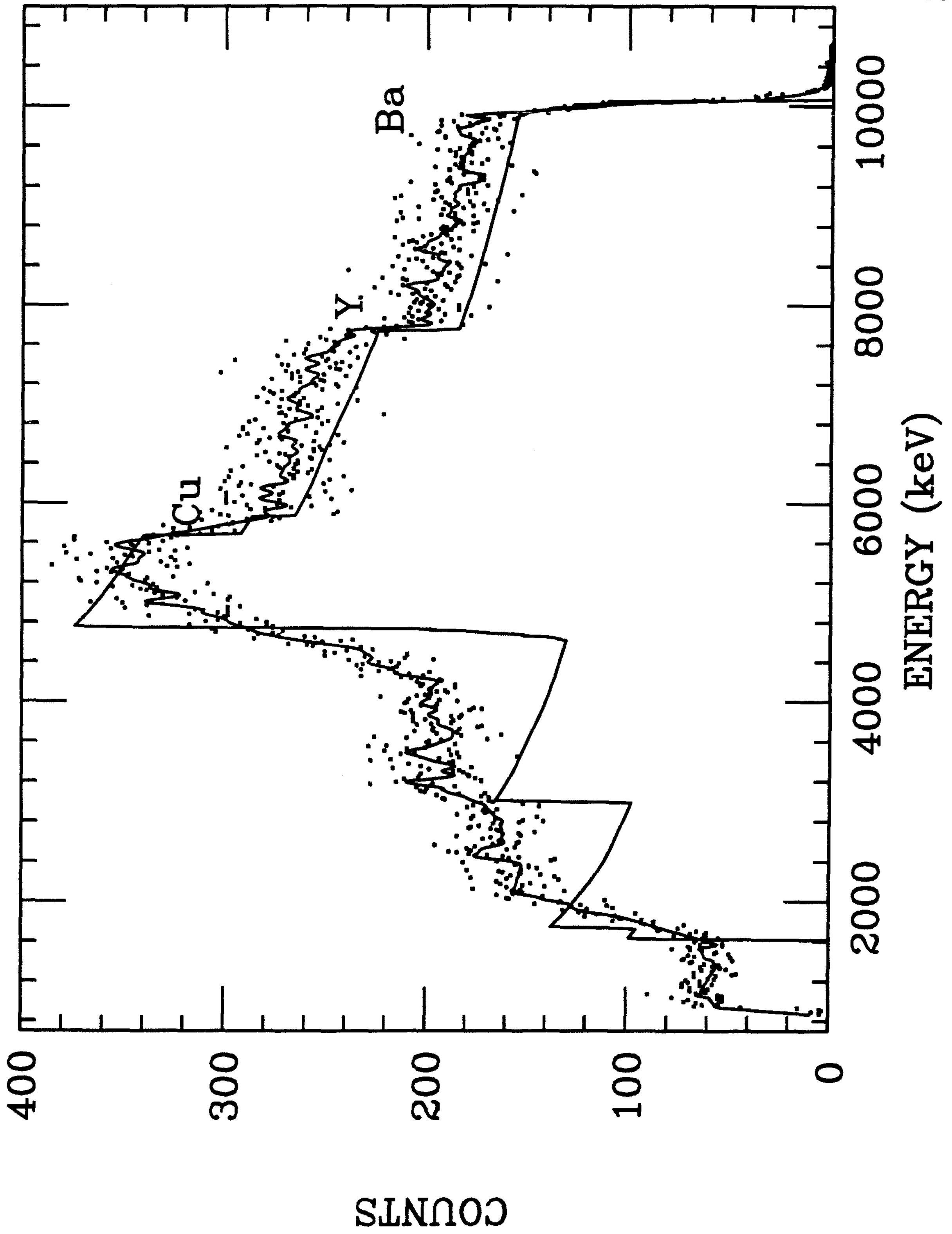

Figure 21b

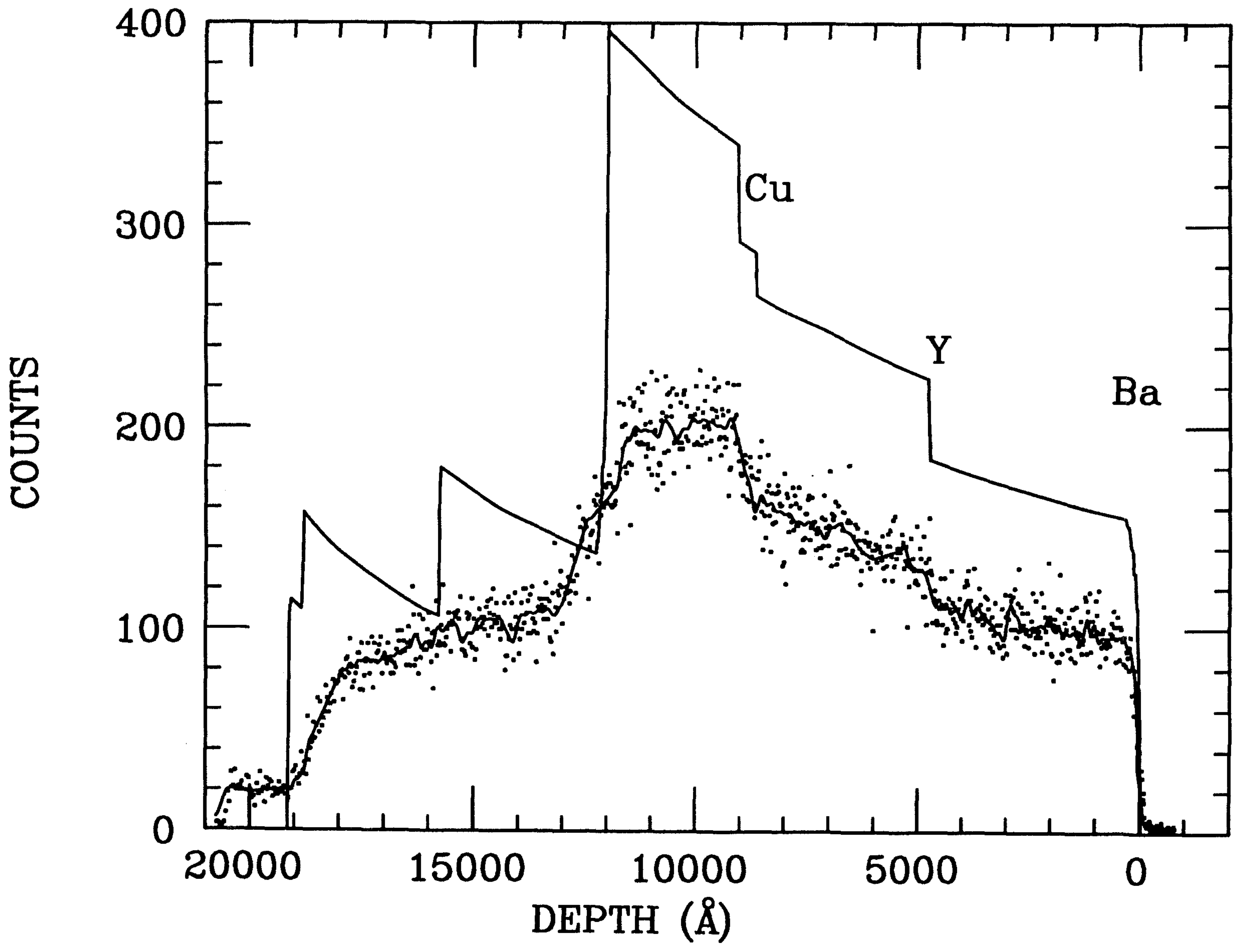

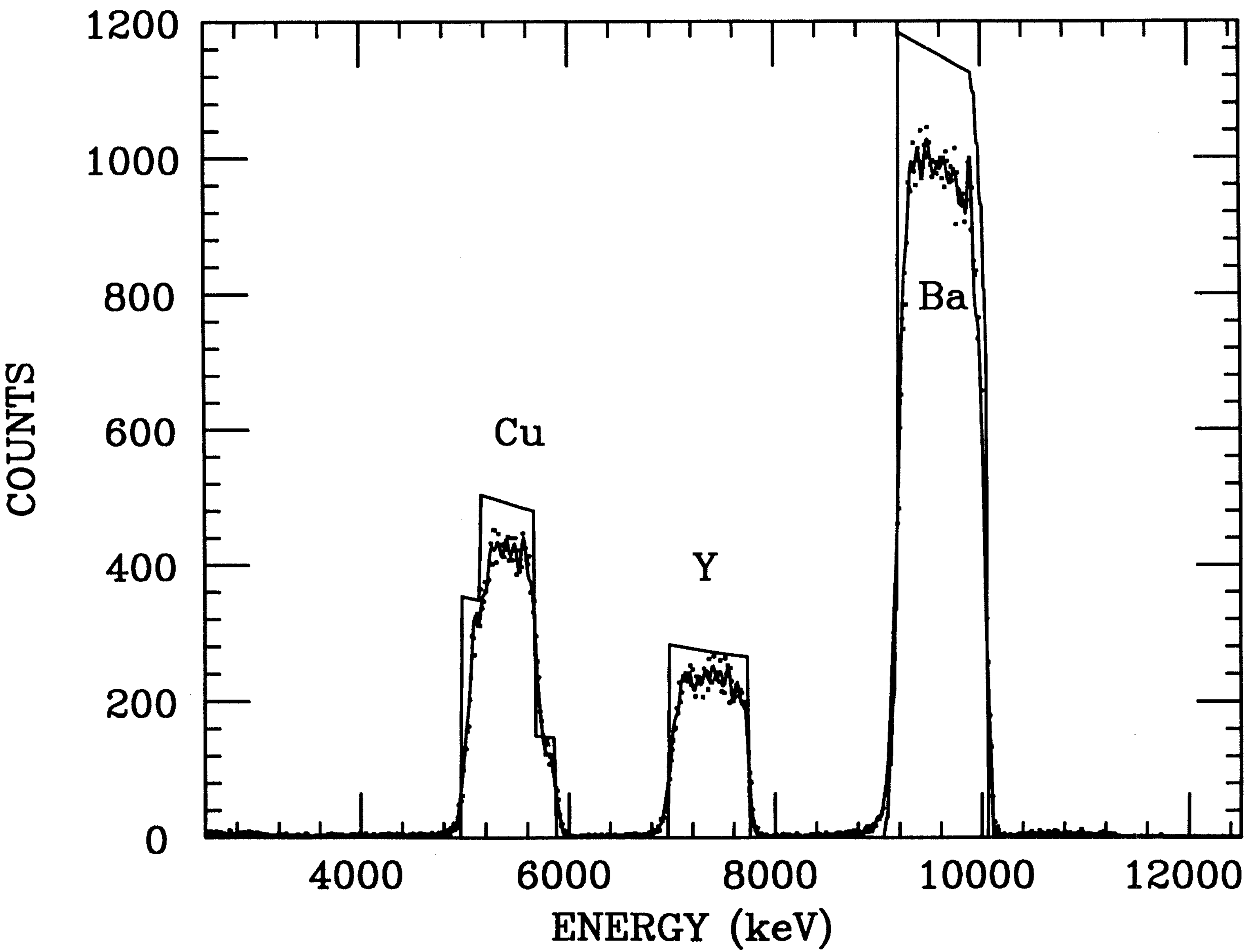
COUNTS
0
200
400
600
800
1000
1200
ENERGY (keV)
4000
6000
8000
10000
12000
Cu
Y
Ba

Figure 22b

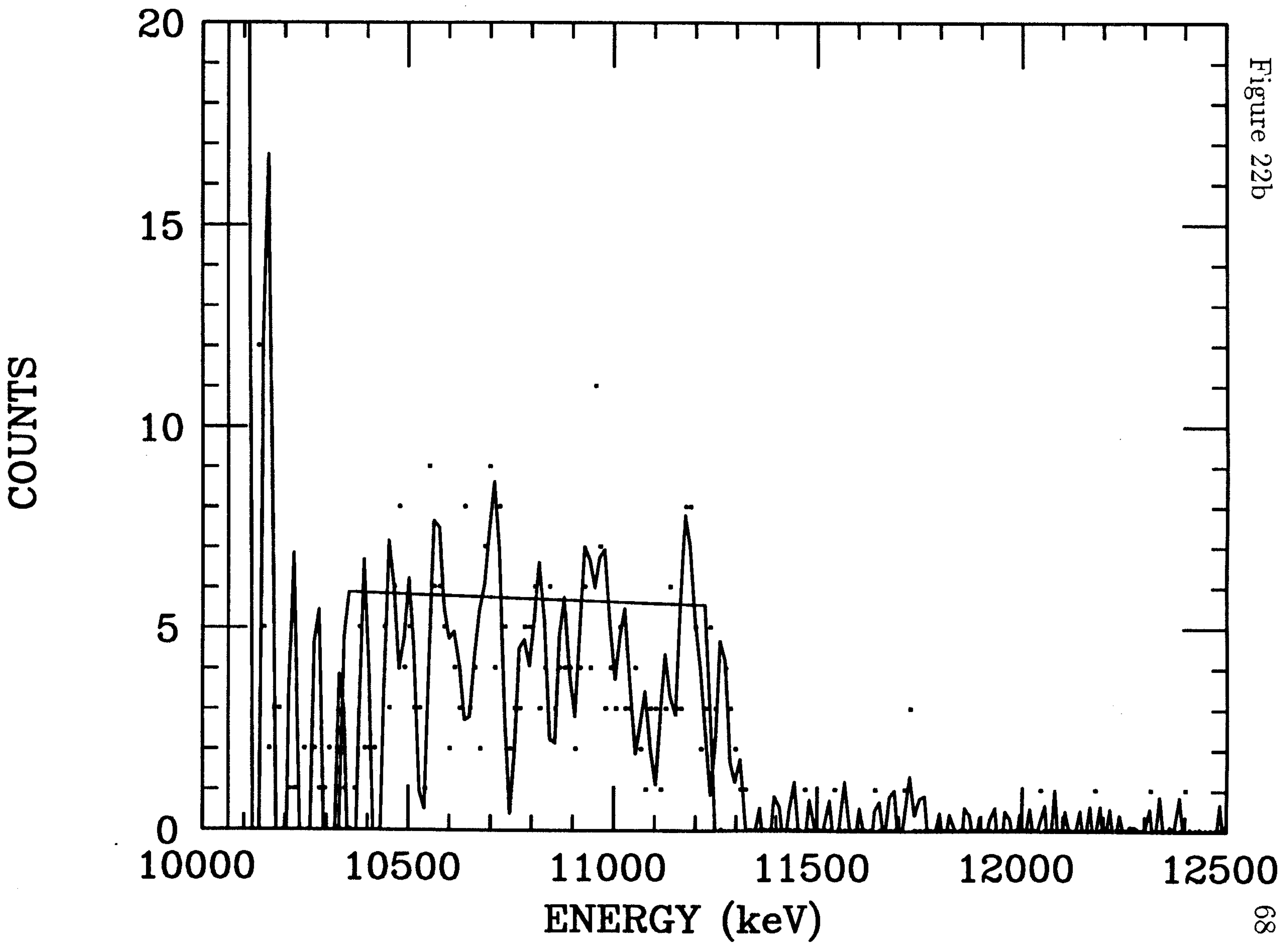

Figure 23a

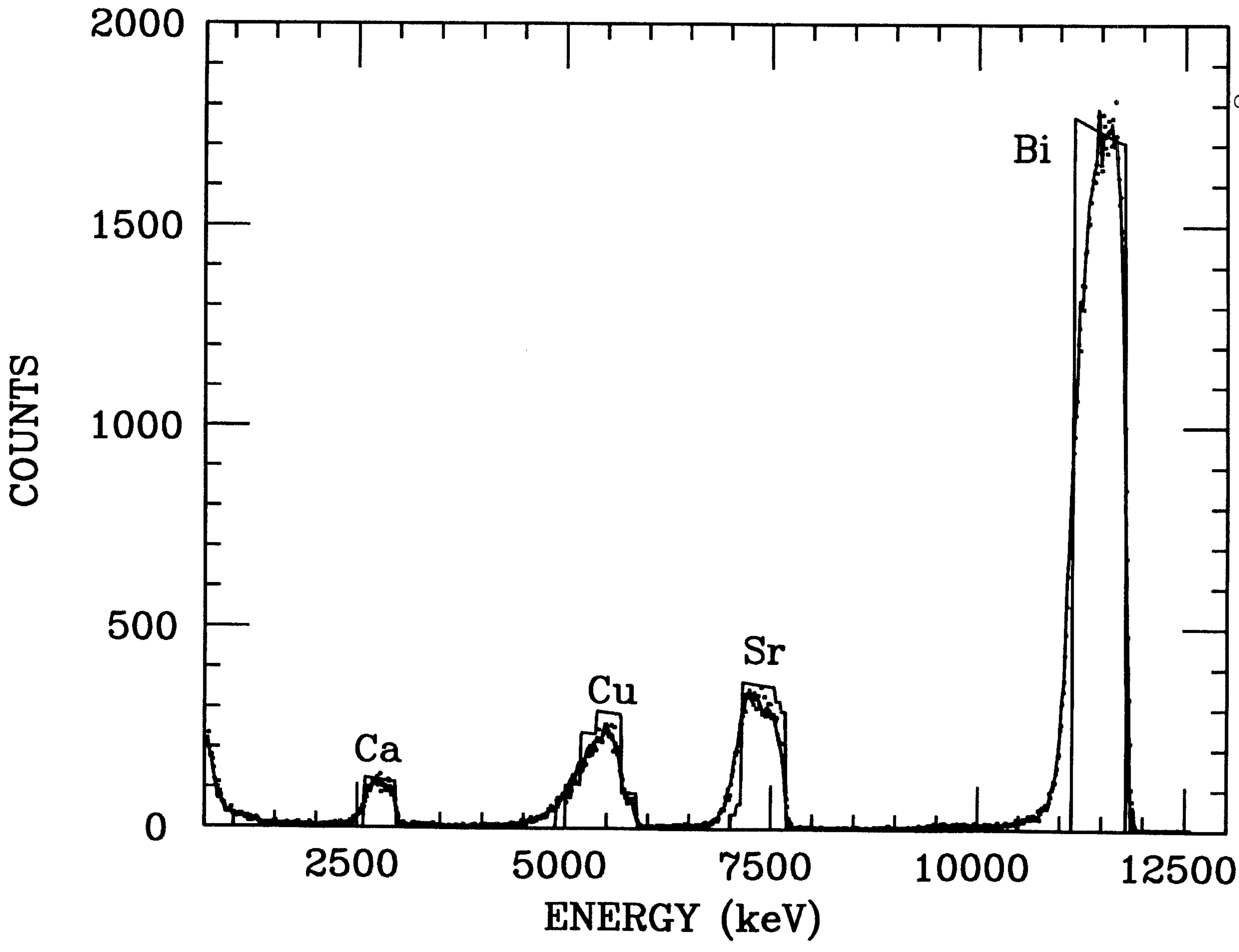

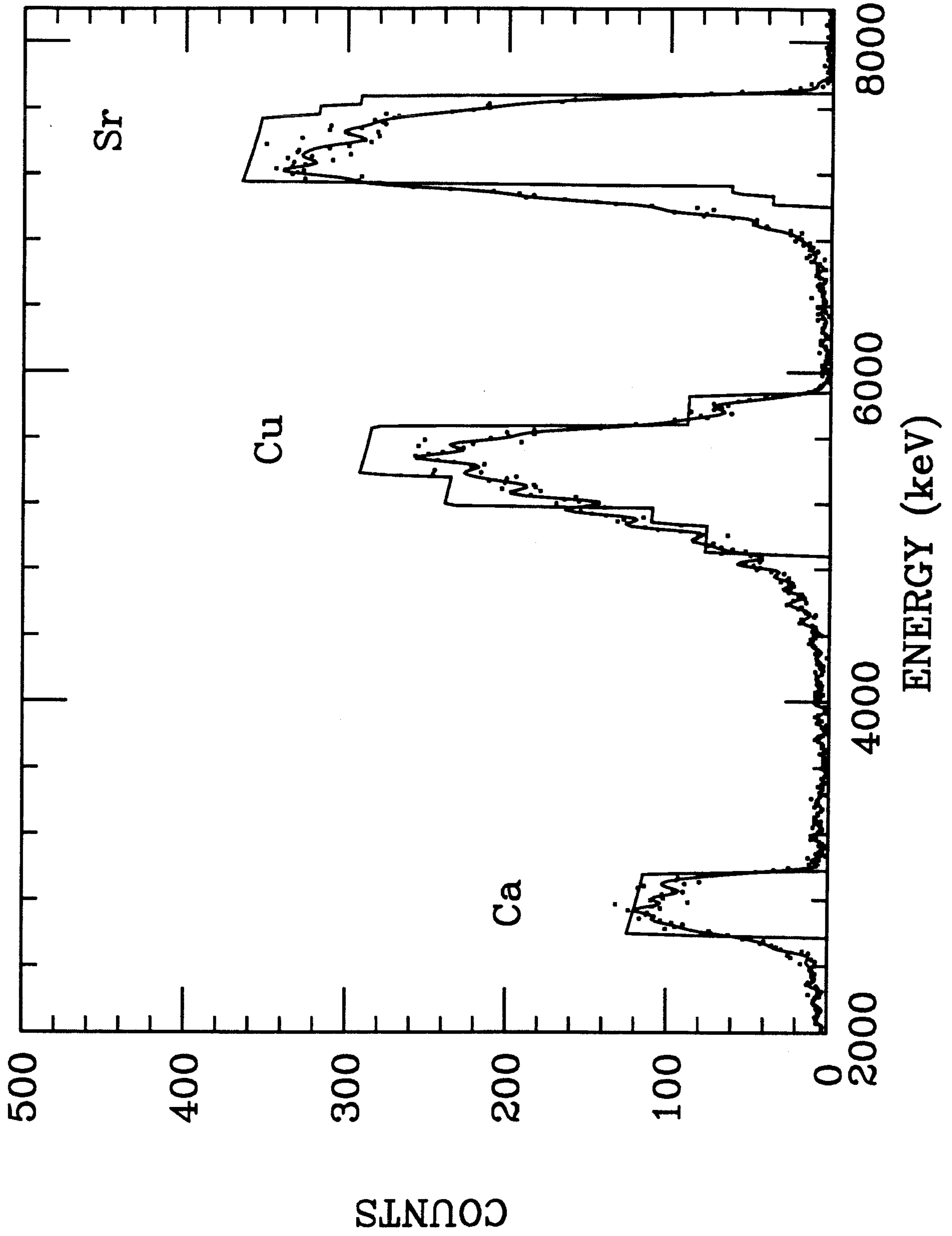
Sr
Cu
Ca
COUNTS
0
100
200
300
400
500
ENERGY (keV)
2000
4000
6000
8000

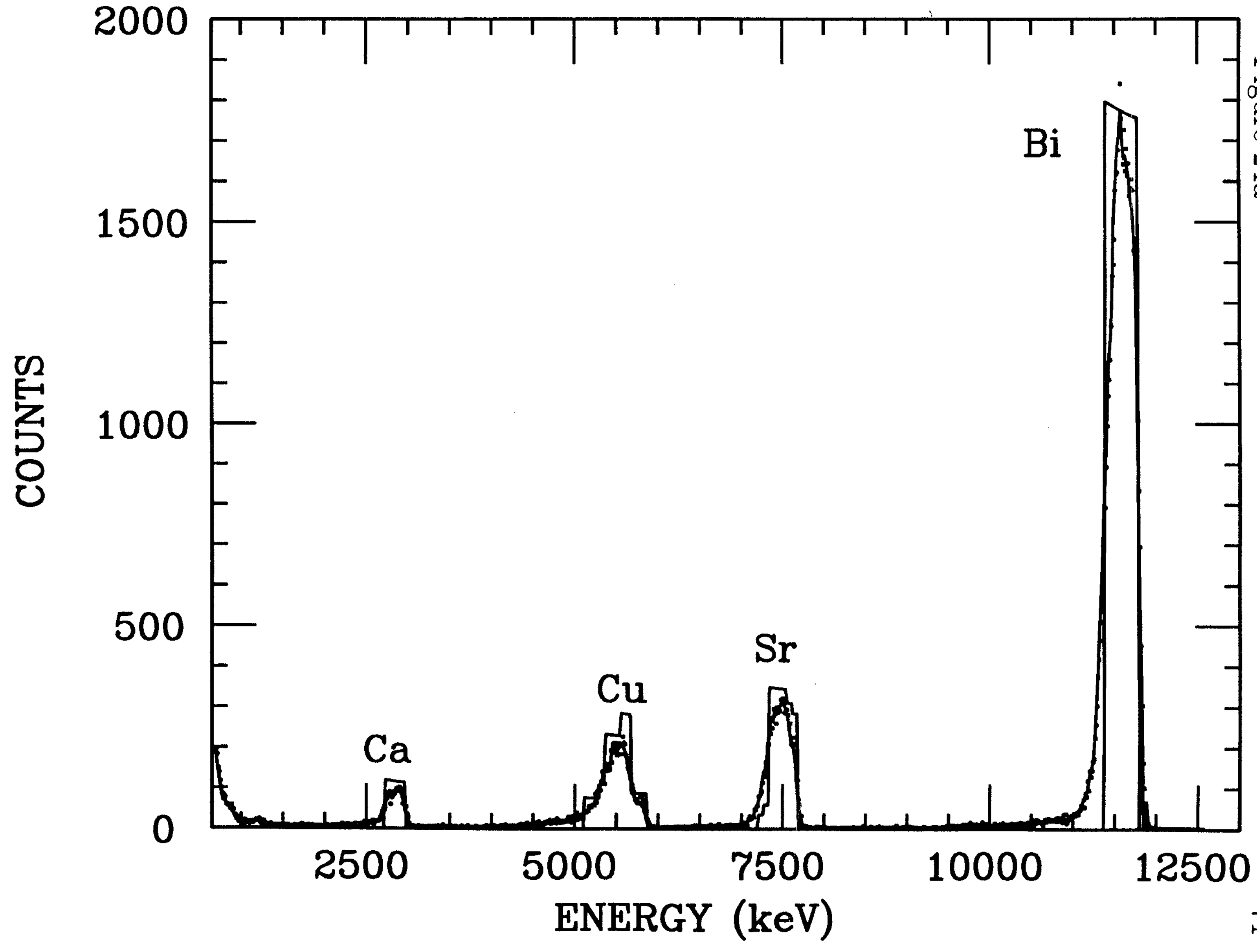
Bi
Sr
Cu
Ca
COUNTS
0
500
1000
1500
2000
2500
5000
7500
10000
12500
ENERGY (keV)

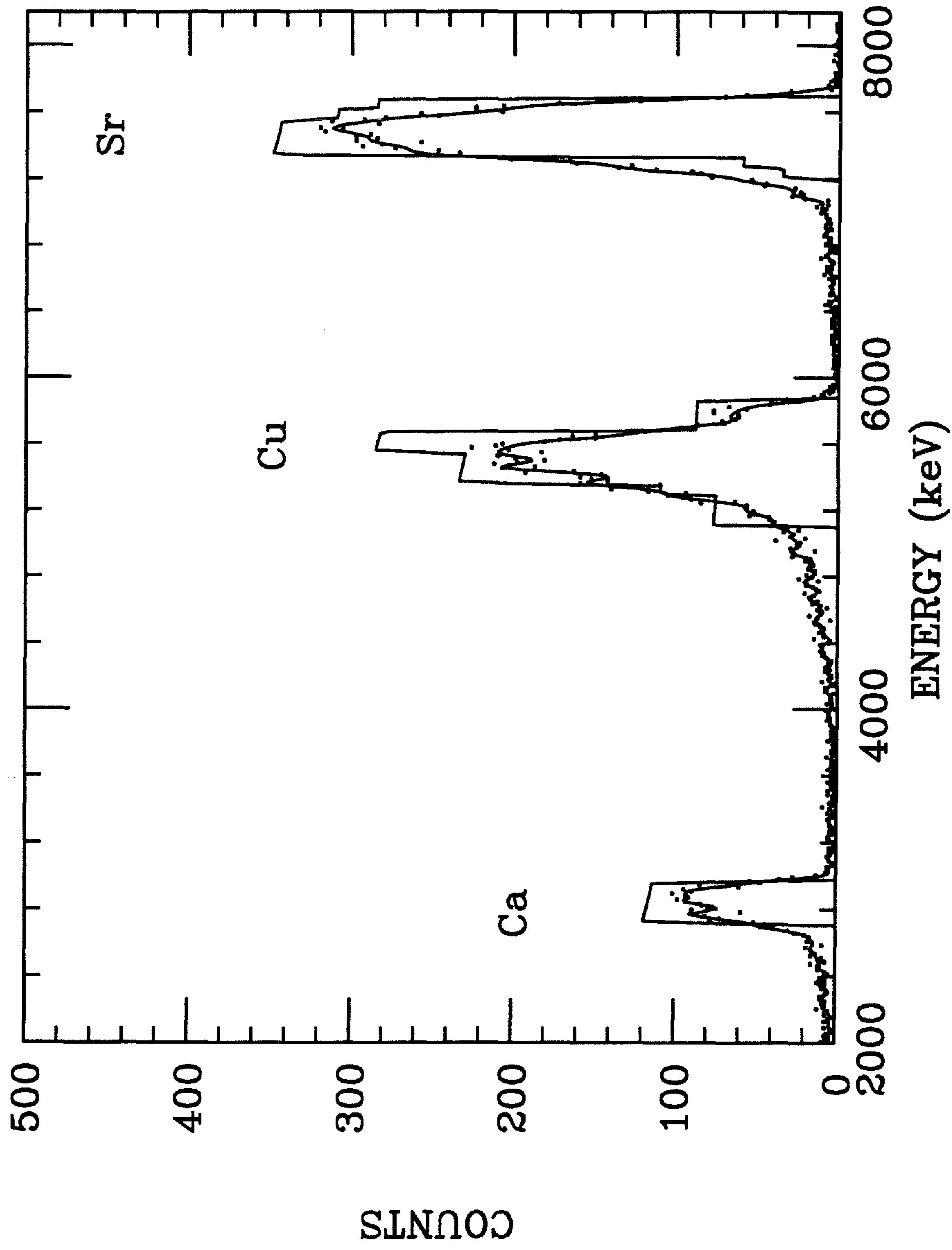
Sr
Cu
Ca
COUNTS
ENERGY (keV)
0
100
200
300
400
500
2000
4000
6000
8000

Figure 25

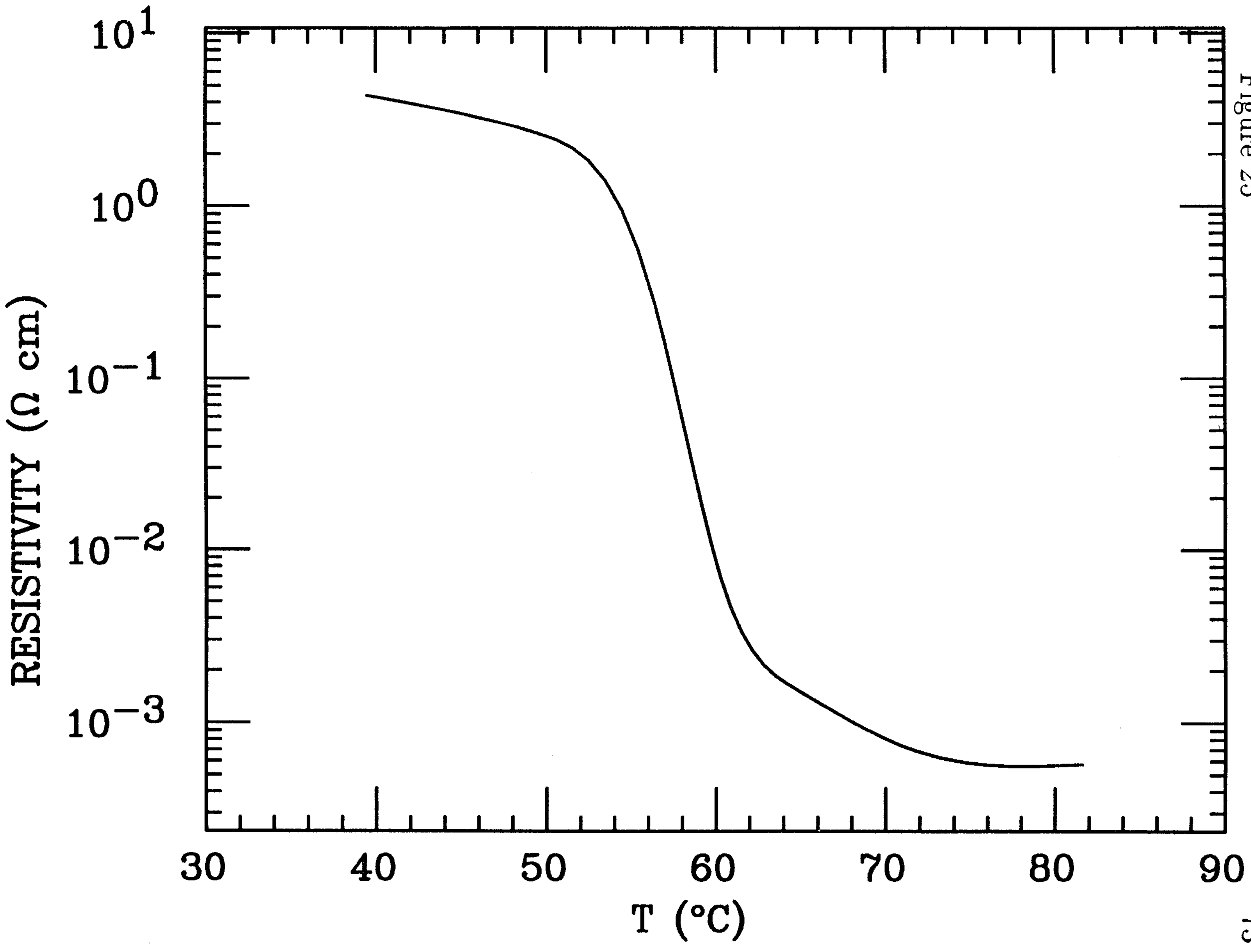

run #	spot #	T [°C]	$N_0[\times 10^{14}]$	raw counts		$N(\theta)[\times 10^{12} \frac{atom}{cm^2}]$		Y	
				15°	25°	15°	25°	15°	25°
1	1	27–37	3.83	363	291	221±14	172±12	4.68±.3	3.86±.3
2	1	75–128	3.74	140	131	68.2±9	41.4±9	1.48±.2	1.43±.2
3	2	75	3.74	83	97	29.1±8	38.7±8	.63±.16	.89±.2
4	2	35	3.74	80	58	27.1±8	12±7	.59±.16	.28±.16
5	2	75	12.50	156		79.1±10		.51±.06	

Results of the VO_2 sputtering experiment. N_0 is the number of incident Cl ions, $N(\theta)$ is amount of V on the collector foil, and Y is the estimated total yield. 15° and 25° refer to locations on the collector foil corresponding to those ejection angles from the sample.

	$\frac{\partial Y}{\partial \Omega}$							
	cold				hot			
angle	total	V	Ni	W	total	V	Ni	W
15	1.45±.09			.06±.005	.2±.05			.007±.002
20	1.14±.06	.99±.05	.15±.03	.07±.004	.32±.04	.21±.03	.11±.03	.008±.001
25	1.13±.08			.05±.004	.26±.05			.004±.002
30	1.02±.06	.88±.05	.15±.03	.05±.003	.25±.04	.15±.03	.11±.03	.006±.001
40	1.21±.06	1.08±.06	.12±.03	.05±.003	.28±.04	.14±.03	.13±.03	.002±.001
50	1.33±.06	1.22±.06	.11±.03	.04±.003	.27±.04	.12±.03	.15±.03	.006±.001
60	.89±.05	.74±.05	.15±.03	.02±.002	.15±.04	.06±.03	.1±.03	.002±.001
70	.79±.05	.72±.05	.07±.02	.02±.002	.21±.04	.08±.03	.13±.03	.002±.001
80	.89±.05	.83±.05	.06±.02	.02±.002	.28±.04	.15±.03	.13±.03	.005±.001
85	1.04±.06	.98±.05	.05±.02	.03±.002				.005±.001
90	.91±.05	.9±.05	0±.02	.05±.003	.14±.04	.11±.03	.03±.02	.003±.001

Angular dependence of differential yield for the cold and hot runs done on virgin surfaces. $\frac{\partial Y}{\partial \Omega}$ is the number of sputtered particles per unit solid angle per incident ion. 'V' is from the counts in the Vanadium peak, 'Ni' is something about eight mass units heavier, 'W' is likewise something in that neighborhood of mass.

Figure 28a

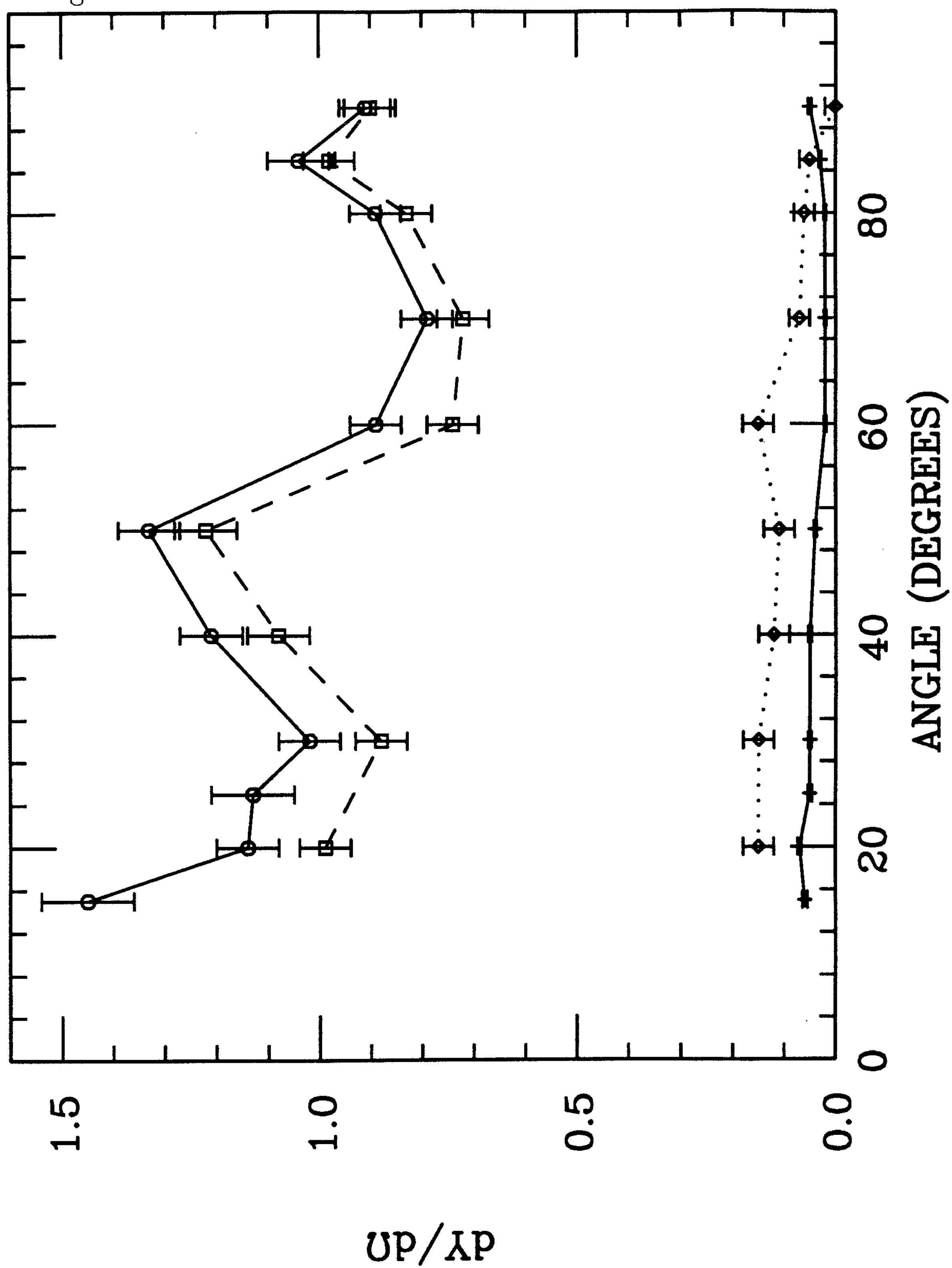

Figure 28b